THE ASTROPHYSICAL JOURNAL, 302:306–336, 1986 March 1

THE RADIO GALAXY IC 4296 (PKS 1333−33). I. MULTIFREQUENCY VERY LARGE ARRAY OBSERVATIONS

N. E. B. KILLEEN
Mount Stromlo and Siding Spring Observatories, Research School of Physical Sciences, Australian National University, and the National Radio Astronomy Observatory[1]

G. V. BICKNELL
Mount Stromlo and Siding Spring Observatories, Research School of Physical Sciences, Australian National University

AND

R. D. EKERS
National Radio Astronomy Observatory
Received 1985 April 23; accepted 1985 August 26

ABSTRACT

We present Very Large Array (VLA) observations of the E1 radio galaxy IC 4296 (PKS 1333−33) at 1.3, 2, 6, and 20 cm, with a best (usable) resolution of 3".2. The source consists of an unresolved core (coincident with the nucleus of IC 4296) from which issue two symmetric, curved jets. Both jets terminate in slightly edge-brightened lobes. The total extent of the source is approximately 35' (360 kpc, for $H_0 = 100$ km s^{-1} Mpc^{-1}), with the western lobe situated at a projected distance from the core of approximately 130 kpc compared with approximately 190 kpc for the eastern lobe.

Close to the core the jets are unresolved (at 3".2 resolution) and faint. However, at approximately 15" (2.6 kpc) angular distance from the core (Θ), they rapidly flare and brighten. The expansion of both jets slows beyond $\Theta \approx 35''$ (6.0 kpc). The spectral index in each jet is steep initially (at $\Theta \approx 8'' = 1.4$ kpc), but flattens as the jets widen and brighten, and is approximately constant exterior to $\Theta \approx 60''$ (10.2 kpc). A train of knots in the range $5'' < \Theta < 60''$ (0.9–10.3 kpc) occurs in both jets. Transverse oscillations are apparent in both jets beyond $\Theta \approx 60''$.

There are no large rotation measure gradients apparent in either the jets or the lobes. Interior to $\Theta \approx 18''$ (3.1 kpc), the projected magnetic field in each jet is dominated by the longitudinal component. However, in the region $\Theta \gtrsim 18''$, the field in both jets is transverse. Beyond this magnetic field transition point, the degree of polarization rises from its minimum of approximately 5% and reaches approximately 40% by $\Theta \approx 60''$. There is no evidence for depolarization in the jets of this source. The degree of polarization is typically 20%–30% in the eastern lobe and 10%–15% in the western lobe.

Subject headings: galaxies: individual — galaxies: jets — galaxies: structure — polarization — radio sources: galaxies

I. INTRODUCTION

Radio jets are a well-established phenomenon in a large number of extragalactic radio sources. There exist VLBI jets on a scale of a few parsecs (e.g., Readhead, Cohen, and Blandford 1978; Linfield 1981, 1982) and large-scale jets with sizes of hundreds of kiloparsecs (see the reviews by Miley 1980; Bridle and Perley 1984). These jets are presumed to define paths over which energy is transported from the core to the extended lobes. However, apart from this rather general statement, no consensus exists on the nature of their detailed physics. Five outstanding problems have been identified:

1. What determines the spreading rate of a jet?
2. What causes the rapid brightening or "turn on" of jets a few kpc from their cores?
3. What determines the usually slow decline of surface brightness?
4. What is the velocity of a jet?
5. What is the energy flux in a jet and in what form does it occur?

In general, simple magnetohydrodynamic models are inadequate to address these problems since they imply a rapid decrease of surface brightness with increasing jet radius (e.g., see Bridle 1982). Turbulence or repeated shocks in a supersonic flow may be responsible for the observed morphology, surface brightness, or both (Bicknell 1984; Norman *et al.* 1982), but no definitive theoretical model exists at the present time.

The accumulation of data on a large number of jets is important since various theoretical ideas can be assessed by observations of particular jets. Moreover, statistical data on the systematics of radio jets (e.g., Bridle and Perley 1984) will undoubtedly lead to a greater physical understanding of the jet phenomenon in general.

In this paper we present multifrequency VLA observations of the radio source PKS 1333−33, which is associated with the elliptical galaxy IC 4296 (see Table 1). This object is relatively nearby and hence an ideal candidate for a detailed study in the radio, optical, and X-ray regimes. Furthermore, its simple radio morphology (compared with, e.g., M87 or Cen A) facilities theoretical modeling. Optical data, X-ray data, and a theoretical interpretation will be presented in subsequent papers. The plan of this paper is as follows. In § II we give a brief

[1] The National Radio Astronomy Observatory is operated by Associated Universities, Inc., under contract with the National Science Foundation.

TABLE 1

OPTICAL PROPERTIES OF IC 4296

Parameter	Value
Hubble type	E1
Magnitude	$B_T = 11.6$
Redshift	$v_0 = 3523$ km s^{-1}
Distance	35.2 Mpc ($H_0 = 100$)
Linear to angular scale	0.171 kpc arcsec^{-1}
Major axis position angle	61°
Right ascension (1950)	$13^h33^m47^s.2$
Declination (1950)	−33°42′39″.4

review of previous radio observations. In § III we discuss our VLA observations, and in § IV we describe the data reduction procedures. In §§ V and VI we present characteristics of the source apparent from the total intensity and polarization maps, respectively. We calculate the equipartition parameters in § VII, and we summarize the main results in § VIII.

II. PREVIOUS RADIO OBSERVATIONS

The bright E1 galaxy IC 4296 was first identified with the radio source now known as PKS 1333−33[2] by Mills, Slee, and Hill (1960). Since then, this source has been extensively observed at low resolution by Gardner and Davies (1964), Schilizzi and McAdam (1970), Gardner and Whiteoak (1971), and Slee (1977). These observations all revealed that the source was comprised of three nearly colinear components, with the central component centered on IC 4296. The nature of the central component became clearer when the source was mapped at 1415 MHz by Goss *et al.* (1977) using the Fleurs synthesis telescope (FST), which provided 50″ resolution. Goss *et al.* described PKS 1333−33 as a double-double radio galaxy, since the central component was itself resolved into a double source. This new structure was also aligned along the overall source axis, with a component on either side of the optical galaxy's nucleus. A compact core radio source was reported by Schilizzi (see Goss *et al.*) at 8.2 GHz and also by Fomalont (see Goss *et al.*) at 2.7 and 8.2 GHz. A 5 GHz VLA survey (Shaver *et al.* 1982; Ekers *et al.* 1985) showed that the central source consisted of a core and two bright, symmetric jets. This observation initiated the present detailed study of this source. Recently, the newly developed Ooty synthesis telescope has mapped this source at 327 MHz with 3′ resolution (Swarup 1984). This map is in reasonable morphological agreement with the Molonglo cross map (Schilizzi and McAdam 1970).

III. VLA OBSERVATIONS

Since PKS 1333−33 is a large source (35′ ≈ 360 kpc, $H_0 =$ 100 km s^{-1} Mpc^{-1}), it is difficult to map completely with the VLA. The most compact VLA configuration has a minimum unprojected antenna spacing of 40 m, which inadequately samples structures larger than 15′ (∼ 154 kpc) at 20 cm, about half the total extent of PKS 1333−33. Thus our maps do not accurately represent the extended large-scale structure of this source, especially in the lobes. Nevertheless, by combining data from different configurations, maps which well represent the jets have been obtained. Owing to the southerly declination of PKS 1333−33, the maximum duration of a single observation was 6 hr. Furthermore, we observed with the north arm in the next larger configuration than the other two arms whenever possible. This produced an approximately round beam. We observed PKS 1333−33 at four frequencies with three VLA configurations. Table 2 lists the main observing parameters.

The observations were calibrated by short, regular (typically every ½ h) observations of the nearby source 1313−333, whose flux density was then scaled with that of the standard source 1328+307 (3C 286) on the system of Baars *et al.* (1977). These observations were further used to calibrate the instrumental polarization parameters of the antennas. The polarization position angle zero point was set by assuming that the position angle of 3C 286 was 33° at all frequencies.

Ionospheric Faraday rotation can be an important effect at 20 cm. Nevertheless, it was found (see § VI*a*) that the electric vector position angles in all the individual 20 cm polarization maps were consistent with each other to within approximately 5°–10°, indicating that the ionospheric effect was minimal. However, small position angle changes of this magnitude can produce some apparent depolarization (see § VI*c*).

The $D + C_n$ (the subscript refers to the configuration of the north arm) 20 cm data were ruined by solar interference and provided no useful information at the short baselines for which they were primarily intended. These data are not discussed further.

IV. DATA REDUCTION

Following calibration, all reductions were completed with the NRAO Astronomical Image Processing System (AIPS).

Ionospheric and atmospheric phase fluctuations often severely reduce the dynamic range of an aperture synthesis map. PKS 1333−33 contains an unresolved core source (flux density greater than 0.15 Jy at all frequencies) centered on the optical galaxy, and it was possible to correct some of the data for such phase irregularities by using the core as a phase reference (Schwab 1980). This technique requires that the jets be resolved from the point source on long baselines, and therefore could not be used on the 20 cm C, C + A_n, and D + C_n configuration observations. Table 2 indicates which data sets were self-calibrated using this method.

After the self-calibration and mapping procedures, all "dirty" maps were deconvolved using the CLEAN (Högbom 1974) algorithm as implemented by Clark (1980).

As mentioned in § III, short-spacing information is missing from some of our data. It is possible to insert a zero spacing value during the mapping process to assist CLEAN in its interpolation of the missing data. For example, the 6 cm observations of the lobes (see § V for details) suffer from missing spacings, and the appearance of the maps is vastly improved by the inclusion of a zero spacing value. However, it is still unlikely in this and other cases that all the extended structure has been accurately reconstructed. This is because of the large difference between the zero spacing value and the maximum amplitude of the visibility function, which is reached at the minimum VLA spacing.

In some cases it was desirable to produce a map with lower resolution than the best possible. This was done by applying a taper in the (u, v) domain.

Finally, the CLEANed maps were corrected for the attenuation caused by the primary beam. This is important for such a large source, especially at 6 cm.

[2] The Parkes catalog lists the entire radio source as three separate components: PKS 1332−33, 1333−33, and 1334−33. PKS 1333−33 is strictly associated only with the core source and jets, while PKS 1332−33 and PKS 1334−33 are identified with the western and eastern lobes, respectively.

TABLE 2

VLA OBSERVING PARAMETERS

Parameter	1981 Oct 10	1981 Oct 10	1981 Oct 10	1981 Oct 10	1981 Oct 9	1981 Nov 7	1981 Nov 7	1981 Nov 7	1981 Nov 20	1982 Jan 28	1982 Jul 9	1982 Jul 10
Field center (1950)[a]	core	wlob	core	elob	core	core	core	elob	core	core	core	core
Configuration[b]	D + C_n	D + C_n	D + C_n	D + C_n	D + C_n	C	C	C	C	C + A_n	B + A_n	B + A_n
Minimum baseline (m)[c]	40	40	40	40	40	63, 40	63, 40	63, 40	63, 40	63, 210	210	210
Maximum baseline (km)[c]	0.84	0.84	0.84	0.84	0.84	2.8, 0.84	2.8, 0.84	2.8, 0.84	2.8, 0.84	2.8, 9.0	9.0	9.0
Wavelength (cm)	20.5	6.1	6.1	6.1	1.3	20.5	6.1	6.1	2.0	20.5	20.7	6.2
Frequency (MHz)	1465	4885	4885	4885	22485.2	1465	4885	4885	14965	1465	1452.4	4872.6
Bandwidth (MHz)	50	50	50	50	50	12.5	50	50	50	12.5	25	25
Duration (hr)	0.5	2	0.5	2	5.5	1	1	2	5.5	5	4.5	7
Resolution (arcsec)[d]	30	10	10	10	3	10 × 30	3 × 10	3 × 10	1 × 3	10 × 3	3	1
Self-calibrated?[e]	...	no	yes	no	yes	no	yes	no	yes	no	yes	yes

[a] Core: $13^h33^m47^s.18$, $-33°42'39''.4$; wlob: $13^h23^m52^s.70$, $-33°37'23''.0$; elob: $13^h34^m33^s.00$, $-33°51'00''.0$.

[b] VLA configuration. D-configuration is the most compact, and A-configuration has the longest baselines. D + C_n refers to D-configuration with the north arm in C-configuration.

[c] Minimum and maximum projected spacings in meters and kilometers, respectively. If two values are given, then they refer to the southwest (and southeast) and north arms, respectively.

[d] Specifies the best possible resolution that each observation could provide.

[e] Indicates whether the data base has been self-calibrated. Ellipsis dots (...) indicate that the data were unacceptable and not presented in this paper.

V. TOTAL INTENSITY DATA

a) Morphology

i) *Large-Scale Structure*

The large-scale structure is best represented by the combination of the C– and C + A_n–configuration 20 cm observations (Fig. 1, and for a color radiograph of a similar map, see the cover of *Scientific American*, Vol. **246**, No. 5 [1982]). This map was produced with a 14 Jy zero spacing (Goss *et al.* 1977) and a heavy taper providing a 60″ FWHM circular beam to emphasize the low surface brightness lobes. Figure 2 (Plate 10) is a superposition of Figure 1 on the optical field (taken from the ESO B survey). This map agrees well with that of Goss *et al.*, given the greater sensitivity of the VLA compared with the FST. The jets are bent as noted by Goss *et al.*, presumably as a result of the motion of IC 4296 with respect to the intergalactic medium. Note that the eastern jet does not traverse its full length at a constant projected curvature. At approximately 270″ (~46 kpc) angular distance from the core (Θ) this jet bends northward and straightens before entering the lobe. This behavior is not evident in the brighter western jet, which continues at approximately constant projected curvature before terminating in its lobe. Figure 3 shows the mean trajectory of the jets measured from Figure 1 at large Θ, and from the higher resolution data of Figures 8 and 10 (see below) at small Θ.

Both lobes are mildly edge brightened, although neither contains a "hot" spot such as those observed in Cyg A (e.g., Perley, Dreher, and Cowan 1984). However, the eastern lobe does have a less intense localized region at its edge which might be termed a "warm" spot. The slight bulge in the contours of the southwestern region of the western lobe is a confusing point source in the field. The total flux density in the 20 cm map is approximately 14.5 Jy, which corresponds to a luminosity of approximately 2.5×10^{41} ergs s^{-1} assuming a spectral index of $\alpha = 0.6$ for the entire source, and frequency cutoffs of 10^7 and 10^{11} Hz.

All of the features in this combined map are present in separate maps made from the C + A_n– and C–configuration 20 cm data sets as well as from the relevant 6 cm data, and therefore are not artifacts of limited (u, v) coverage.

The lobes were mapped in separate observations at 6 cm. D + C_n– and C–configuration observations were obtained for the eastern lobe, and a D + C_n–configuration observation of the western lobe was made. Since these lobes are of low surface brightness, the maps were heavily tapered, and zero spacing values of 2.19 and 3.05 Jy for the western and eastern lobes, respectively, were included (Shimmins, Manchester, and Harris 1969). Figures 4 and 5 (Plate 11) show the eastern lobe at 6 cm with a beam FWHM of 26″. This map was made from the combined D + C_n– and C–configuration data sets. For illustra-

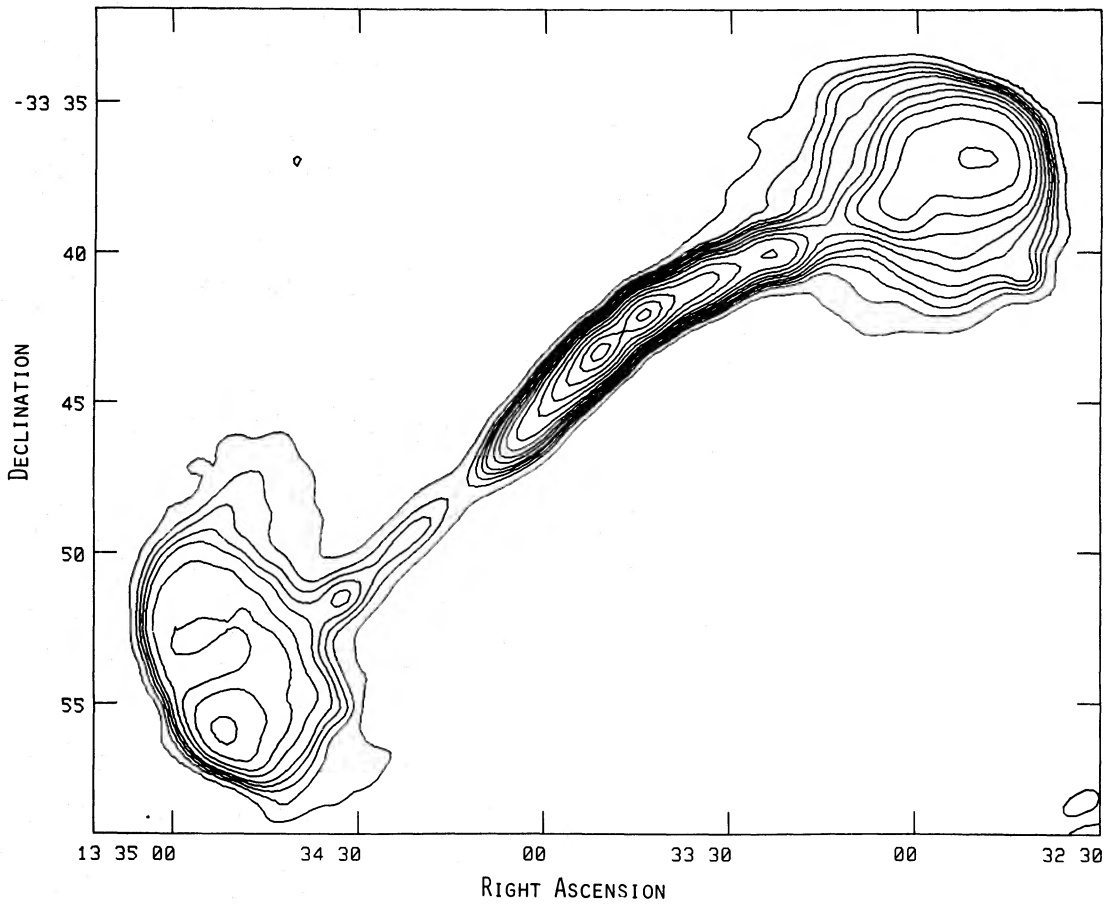

FIG. 1.—Entire source at 20 cm with a 60″ FWHM beam made from the C– and C + A_n–configuration data sets. Peak flux is 778.1 mJy per beam, and the contour levels are −3%, −1.5%, 1.5%, 3%, 4%, 5%, 6%, 8%, 10%, 13%, 17%, 25%, 35%, 50%, 70%, and 90% of the peak. Noise in the map is approximately 1.2 mJy per beam.

PLATE 10

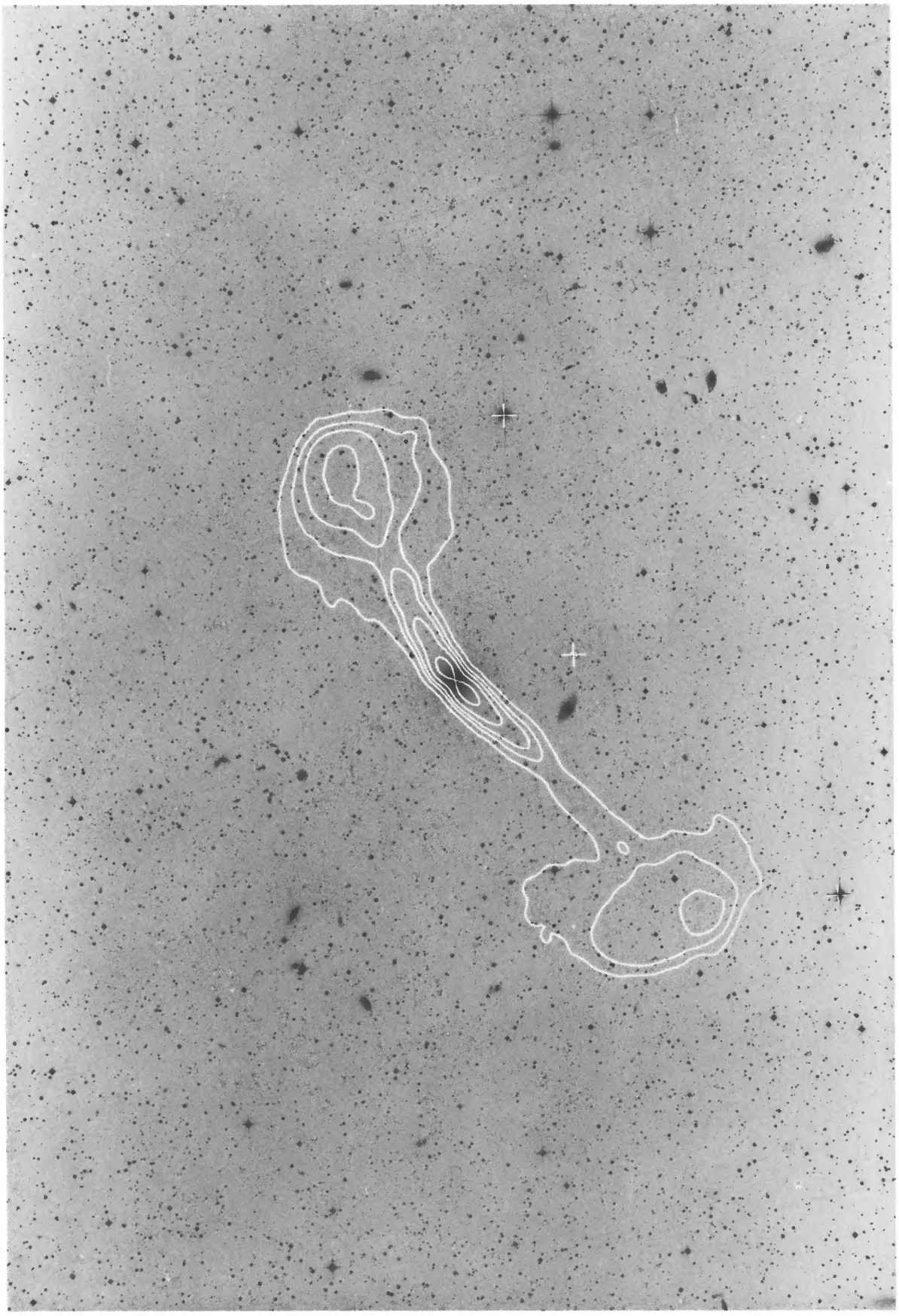

FIG. 2.—The 60″ resolution 20 cm map overlaid on the ESO *B* survey field of IC 4296

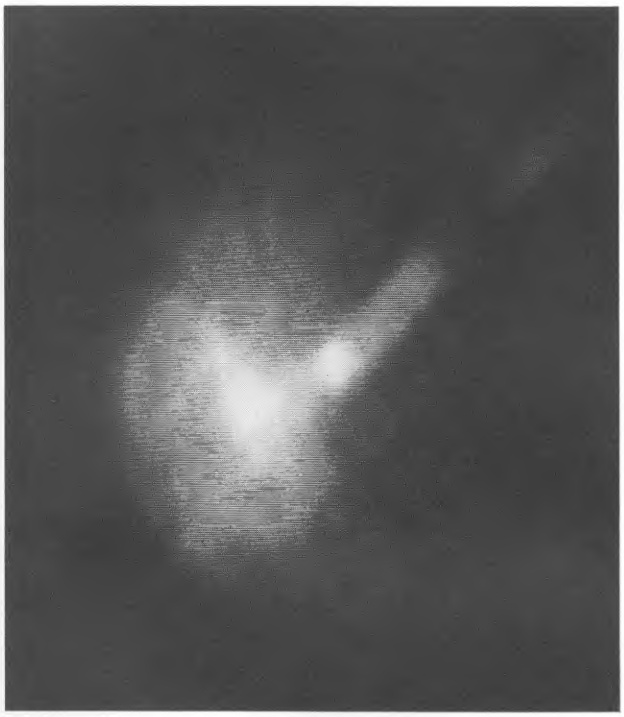

FIG. 5.—Radiograph of the eastern lobe at 6 cm with 26″ resolution. This image has not been primary beam corrected for display purposes only. However, the primary beam correction is substantial at the eastern edge of the lobe (the field center is close to the knot where the jet and lobe merge).

KILLEEN (*see* page 309)

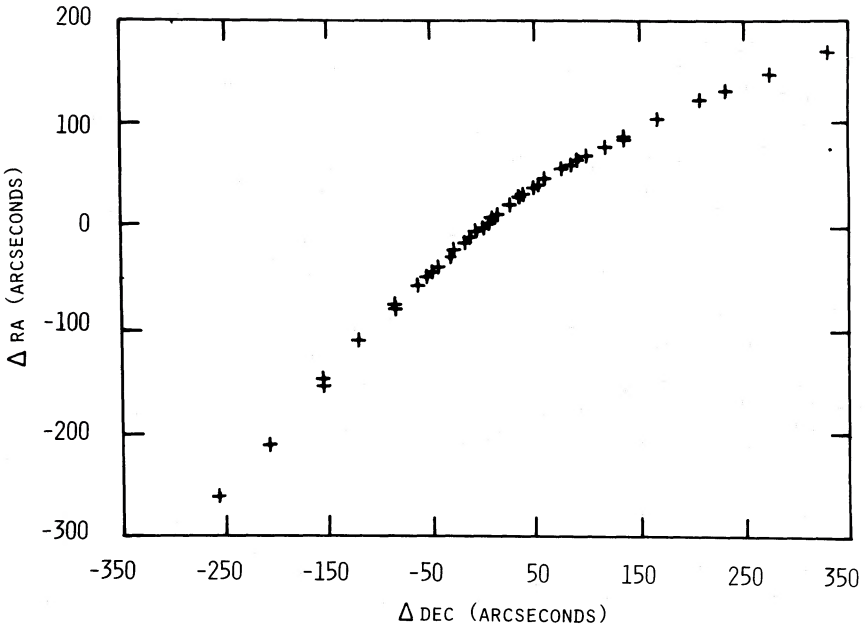

FIG. 3.—Mean trajectory of the jets. The 60″ resolution map was used at large Θ, and the 10.″4 and 3.″2 resolution maps were used at small Θ.

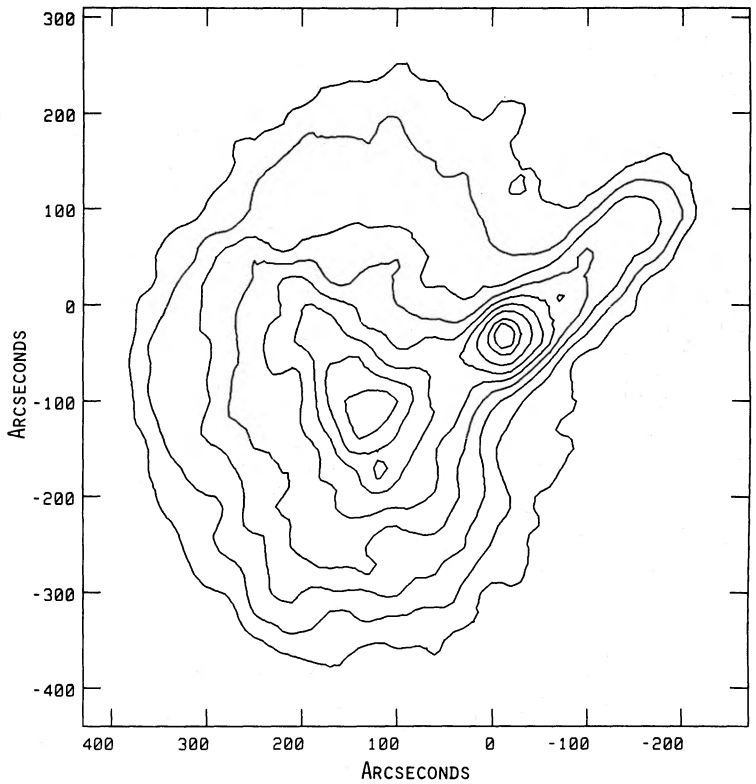

FIG. 4.—Eastern lobe at 6 cm with a 26″ FWHM beam made from the D + C_n– and C–configuration data sets. Peak flux is 8.1 mJy per beam, and the contour levels are −20%, 20%, 30%, 40%, 50%, 60%, 70%, 80%, and 90% of the peak. This map has not been primary beam corrected for illustrative reasons only, and the noise is approximately 1.5 mJy per beam.

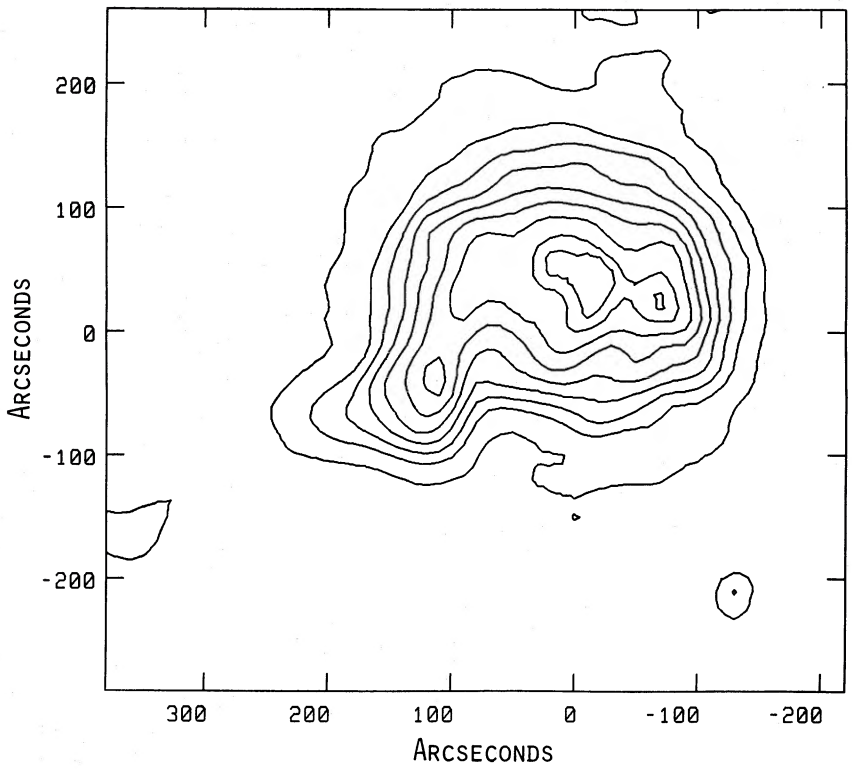

FIG. 6.—Western lobe at 6 cm with a 26″ FWHM beam made from the D + C_n data set. Peak flux is 24.9 mJy per beam, and the contour levels are −15%, 15%, 30%, 40%, 50%, 60%, 70%, 80%, 90%, and 95% of the peak. This map has not been primary beam corrected, and the noise is approximately 1.5 mJy per beam.

tive purposes only, this map and that of Figure 6 have not been primary beam corrected. The noise amplification is too severe toward the lobe edges for a suitable display of the primary beam corrected maps. Figure 4 reproduces the essential features of the lobe visible in Figure 1; in particular, the knot as the jet merges with the lobe. Similarly, Figures 6 and 7 (Plate 12) show the western lobe at 6 cm with 26″ resolution. We note that there is evidence of "shell" or "bubble" structure as the jet traverses the western lobe. This behavior is also discernible in the 20 cm 10.″4 resolution data (see below). However, at this higher resolution, the low surface brightnesses of the lobes preclude a suitable radiograph of the jets and lobes together.

ii) *Jets*

The structure of the jets is revealed by the higher resolution data. Figure 8 displays the 10.″4 resolution map at 20 cm. This map was made with all available multiconfiguration data. The equivalent resolution 6 and 2 cm maps do not show any significant morphological differences from Figure 8, and are not shown in the interest of brevity. The most noticeable features of Figure 8 are the central point source, the "turn on" of the jets close to the core, and the transverse oscillations of both jets. Figure 9 (Plate 13), a radiograph of Figure 8, gives the qualitative impression that these oscillations are helical, rather than transverse deviations from the mean jet direction. There are also regions of surface brightness enhancement as the jet changes direction, most noticeably in the western jet. Section V*e* deals more fully with the oscillations.

Although the projected length of the eastern jet is greater than that of the western jet, it is also fainter. In the 20 cm 10.″4 resolution map (Fig. 8) both jets have integrated flux densities of approximately 2.5 Jy.

In Figures 10 and 11 (Plate 14) we show the best (3.″2) resolution 20 cm map. Only the B + A_n–configuration data were used in this map, since the addition of the shorter baselines would have required prohibitively large maps. The equivalent resolution maps at the other wavelengths are not displayed for brevity. Furthermore, the 1″ resolution 6 cm map does not have sufficient dynamic range to warrant reproduction here. The jets are well resolved from the core at 3.″2 resolution, and they are resolved transversely beyond $\Theta \approx 15''$ (3.4 kpc). An enlargement of the central region of Figure 10 is shown in Figure 12. This clearly shows that the jets are initially unresolved and well collimated, until an apparent rapid flaring and large increase in surface brightness occurs.

Regions of low surface brightness between the cores and jets of several sources (e.g., Butcher, van Breugel, and Miley 1980) have become known as "gaps." In PKS 1333−33 the gap corresponds to the unresolved jets just prior to the rapid expansion and large increase in surface brightness. Butcher *et al.* tabulated the gap lengths in five sources and found them in the range of 0.75–2.2 kpc ($H_0 = 100$). The gaps (east and west) in PKS 1333−33 have a projected length of approximately 2.5 kpc and are thus at the upper end of this range.

Both jets exhibit a train of knots in the region $5'' < \Theta < 60''$ (0.9–10.3 kpc). We have labeled the knots W0–W5 (west) and E1–E5 (east) as shown in Figure 12 (see also Table 3). Although not all these knots show clearly on the contour diagrams, they are easily seen on surface brightness profiles (see Figs. 16*a* and 16*b*).

FIG. 7.—Radiograph of the western lobe at 6 cm with 26″ resolution. This image has not been primary beam corrected for display purposes only. However, the primary beam correction is substantial at the edges of the lobe.

KILLEEN (*see* page 311)

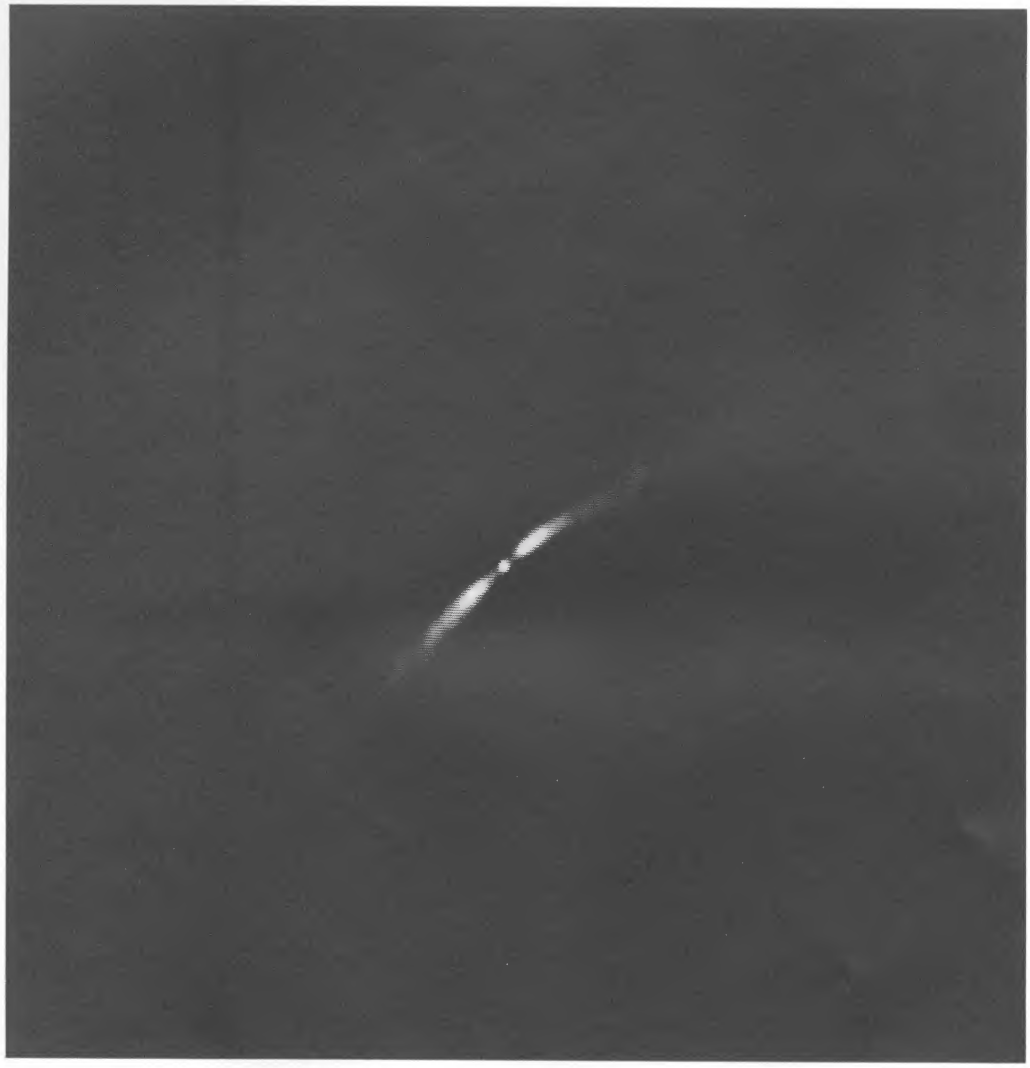

FIG. 9.—Radiograph of the jets at 20 cm with 10.″4 resolution

KILLEEN (*see* page 311)

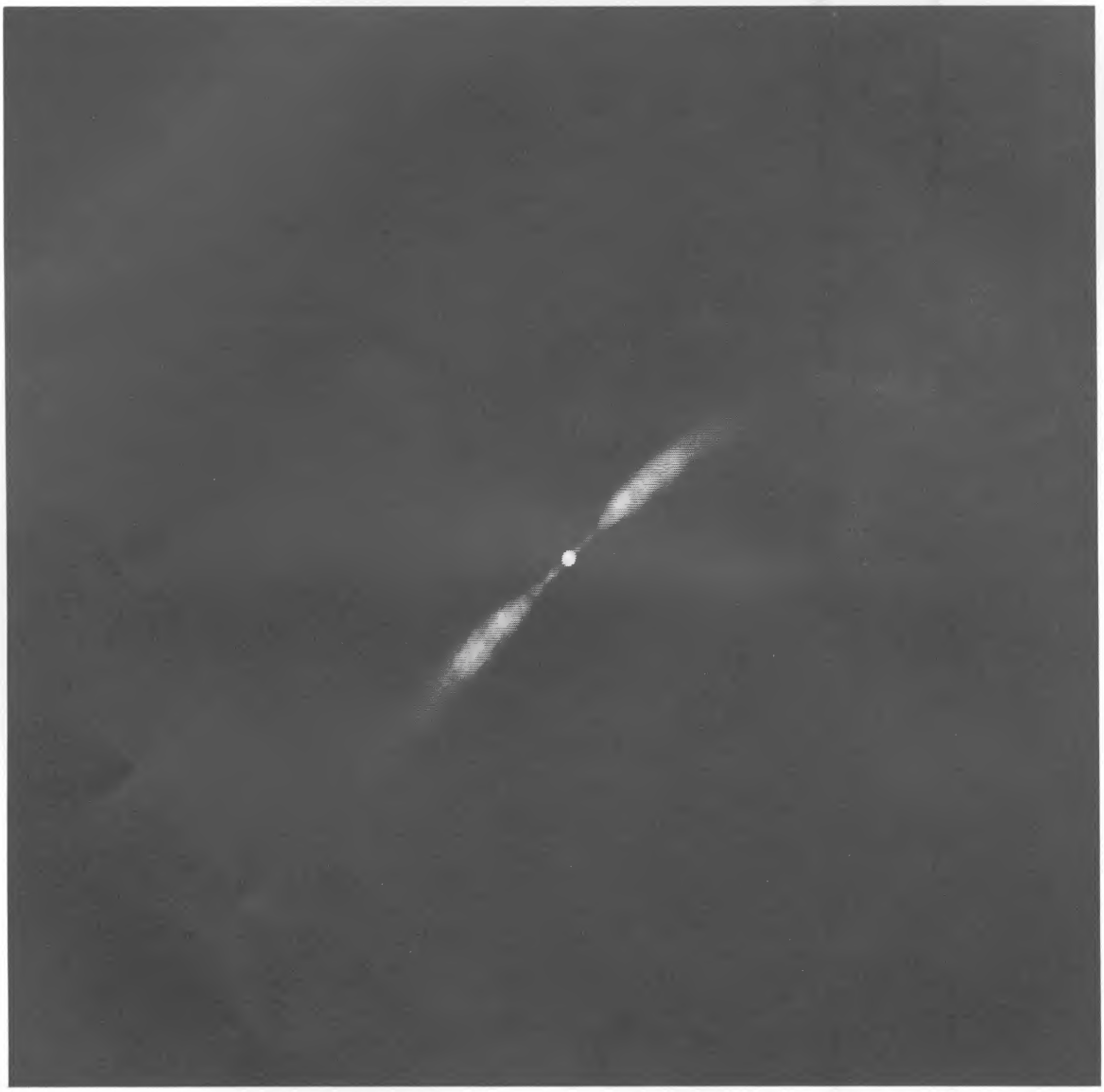

FIG. 11.—Radiograph of the jets at 20 cm with 3″.2 resolution

KILLEEN (*see* page 311)

b) Jet Width

Jets can widen due to turbulence (e.g., Bicknell 1984), the decreasing pressure of a confining atmosphere (Krautter, Henriksen, and Lake 1983), or possibly a combination of both. The variation of the FWHM (Φ) of a jet with angular distance from the nucleus (Θ) is thus an important relation for theoretical modeling of jet behavior. We have made total intensity cross-cuts of the jets in the direction perpendicular to the surface brightness ridge line. Some representative surface brightness profiles are shown in Figures 13*a* and 13*b*. These profiles are well represented by Gaussians, although there is a slight trend for extended wings at large Θ. Some deviation from Gaussians is expected and is found in the regions where the jet oscillates. The main effect of the oscillations is to skew the profiles, especially in the localized regions where the jet undergoes a directional change. Two methods were used to determine the jet widths. (1) A Gaussian was fitted to each profile, deconvolved from the beam (see Appendix A, eq. [A3]), and the FWHM was determined. (2) The area under the profile was calculated, and an equivalent width was evaluated which would reduce to the Gaussian FWHM if the profile were Gaussian. This was again followed by deconvolution as described in Appendix A. Good agreement was obtained between the two techniques, and only method (1) results are presented.

Jet widths were determined from the 3".2 and 10".4 resolution 20 cm maps. The 3".2 resolution data were used for the initial 120" (20.5 kpc) of each jet, and the map at 10".4 resolution was used for the outer jet regions, with some overlap between the two. A slight negative bowl in the 3".2 resolution map was countered by fitting a baseline to each profile and subtracting it before evaluating the FWHM.

In Figure 12 the inner jets are not resolved (for $\Theta \lesssim 15''$), and the full resolution (1") 6 cm data required smoothing to improve their signal-to-noise ratio to a usable level. Thus we can say little about the jet widths in this inner region, beyond that the jets are highly collimated and not expanding at 3".2 (0.6 kpc) resolution.

Figures 14*a* and 14*b* display both the apparent and deconvolved Φ-Θ relation from the 3".2 map for the western and eastern jets, respectively. The deconvolved Φ-Θ data are shown only when the deconvolution criteria described in Appendix A are satisfied. The apparent surface brightness profiles along the jets (see § V*c*) are superposed on the same diagram for comparison. Figures 15*a* and 15*b* show the deconvolved Φ-Θ relation over the first 350" of each jet. There is reasonable agreement between the 3".2 and 10".4 data in the region of overlap, indicating that the deconvolved lower resolution data are not biased by the larger beam. From Figures 14 and 15 it is evident that both jets behave similarly in their collimation properties, although the details vary slightly.

Since the Φ-Θ curves must pass through the origin (on this scale), their behavior for $\Theta \gtrsim 16''$ shows that a change in

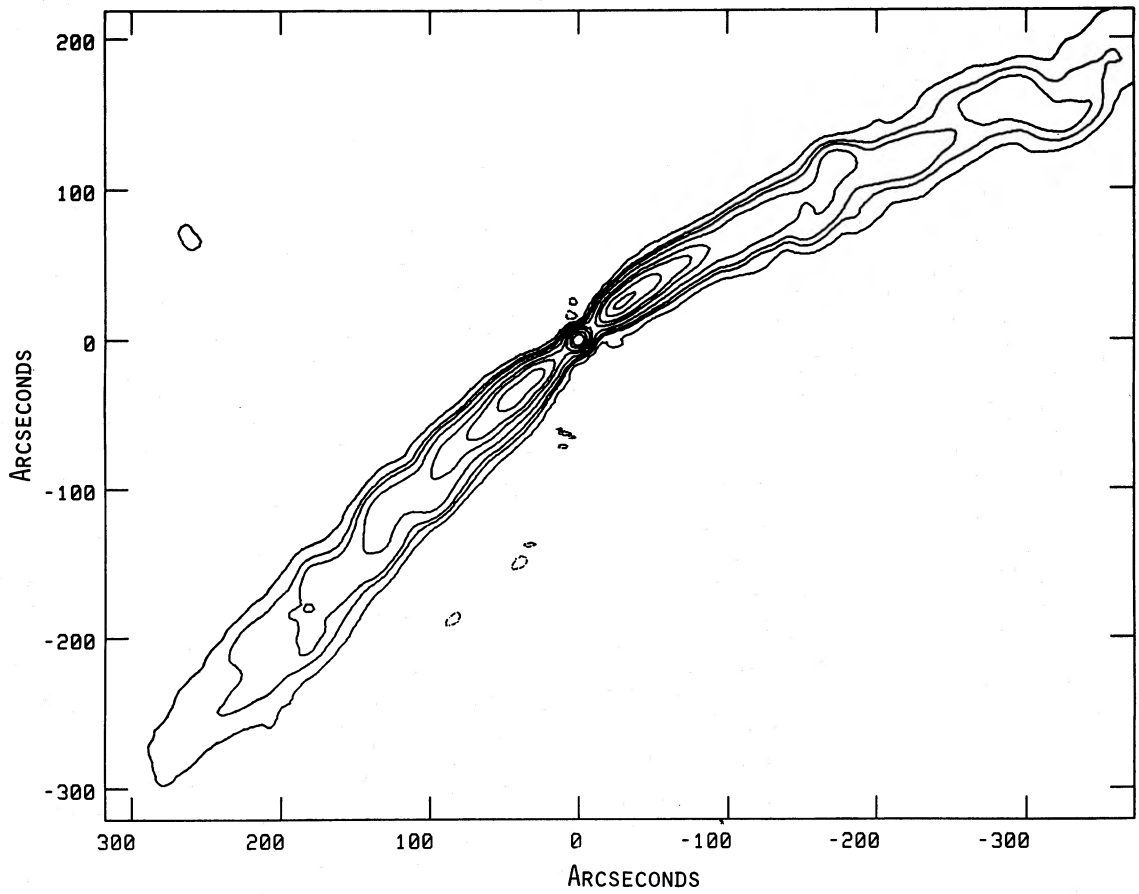

FIG. 8.—Jets at 20 cm with a 10".4 FWHM beam made from the C–, C + A_n–, and B + A_n–configuration data sets. Peak flux is 163.1 mJy per beam, and the contour levels are −3%, −1%, 1%, 3%, 5%, 10%, 20%, 30%, 50%, and 70%, of the peak. Noise in the map is approximately 0.3 mJy per beam.

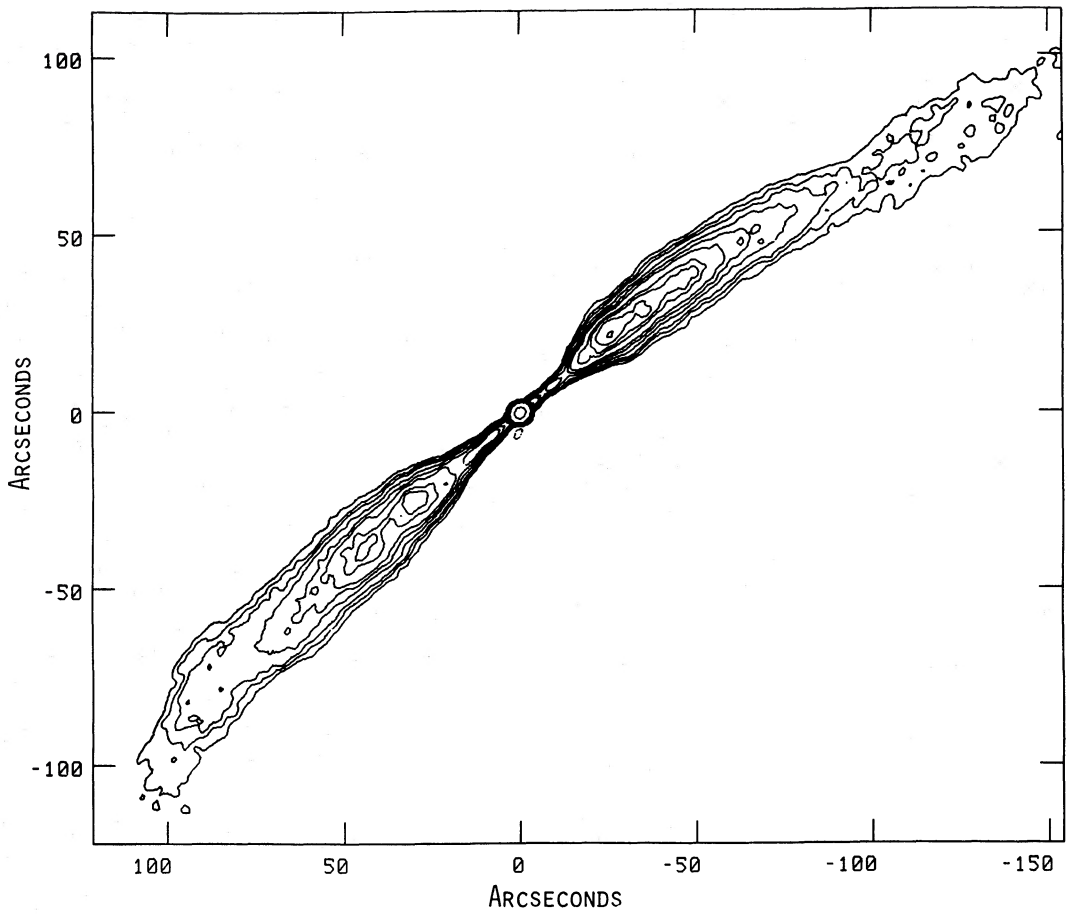

FIG. 10.—Jets at 20 cm with a 3.″2 FWHM beam made from the B + A_n–configuration data set only. Peak flux is 153.1 mJy per beam, and the contour levels are −1%, 1%, 1.5%, 2%, 3%, 4%, 5%, 7%, 8%, 9.5%, 11.5%, and 50% of the peak. Noise in the map is approximately 0.25 mJy per beam.

$d\Phi/d\Theta$ or flaring must occur somewhere in the range $0'' < \Theta < 16''$. However, a quantitative evaluation of the precise location is hindered by inadequate resolution. Initially, the western jet widens rapidly and continues at a constant rate ($d\Phi/d\Theta \approx 0.47$) until $\Theta \approx 35''$ (6.0 kpc). At this point the rapid expansion slows to a rate $d\Phi/d\Theta \approx 0.1$ until $\Theta \approx 110''$ (18.8 kpc). The Φ-Θ curve exhibits small oscillations from $\Theta \approx 30''$–$100''$ (5.1–17.1 kpc). Some of the minima associated with these oscillations can be identified with enhancements in the surface brightness profiles. For example, the minima at $\Theta \approx 48''$, $63''$, and $89''$ (8.2, 10.8, and 15.2 kpc) correspond to knots W4, W5, and the unnamed bump at $\Theta \approx 88''$. Beyond $\Theta \approx 100''$ (17.1 kpc) the expansion rate is less well defined. A continued general expansion at approximately the same rate ($d\Phi/d\Theta \approx 0.1$) is apparent, but superposed are large oscillations of Φ with Θ. Coinciding with these oscillations of the jet width is the onset at $\Theta \approx 110''$ of the transverse oscillations in the jet direction. If the path of the jet in three dimensions is helical, overlapping jet segments may cause false estimates of the jet width by apparent broadening of the profile: This may induce oscillations similar to those of Figures 15*a* and 15*b*. Without knowledge of the three-dimensional nature of the jets, it is difficult to interpret the jet width data in this region.

The expansion of the eastern jet is similar. The deconvolved jet width data (Figs. 14*b* and 15*b*) give an initial expansion rate of $d\Phi/d\Theta \approx 0.42$. Similar to the western jet, small oscillations in the Φ-Θ relation exist when $30'' < \Theta < 100''$, some of which correspond to surface brightness features. The minima at $61''$ and $67''$ (10.4 and 11.5 kpc) correspond with knot E5 and the slight shoulder after its peak, respectively. Also there is a series of small surface brightness peaks in the range $75'' < \Theta < 90''$ with corresponding features in the Φ-Θ diagram. The expansion rate slows at $\Theta \approx 35''$ (6.0 kpc) to $d\Phi/d\Theta \approx 0.1$, similar to the western jet. Once again, there are large oscillations of Φ with Θ at large Θ, coinciding with the oscillations in the jet's direction.

c) Jet Surface Brightness Evolution

The surface brightness (I_ν) evolution of jets is a good indicator of the underlying dynamics. Sudden enhancements of surface brightness can indicate shocks. A smooth, slow decline of surface brightness with jet width may indicate deceleration owing to turbulent entrainment (Bicknell 1984). Alternatively, a decrease of surface brightness in the field-perpendicular region described by $I_\nu \propto \Phi^{(-7\alpha-6)/3}$ (where α is the spectral index; $S_\nu \propto \nu^{-\alpha}$) results from an adiabatically expanding, constant velocity jet (see, e.g., Perley, Bridle, and Willis 1984), which may indicate supersonic flow in which turbulent stresses are unimportant.

For our analysis of the evolution of I_ν with Θ, we have used the same 20 cm maps as were used in the analysis of the jet

widths (see § V*b*). Once again, the 3.″2 resolution map is used for the first 120″ (20.5 kpc) and the 10.″4 resolution map from there on. The 3.″2 and 10.″4 resolution surface brightnesses agree reasonably in the region of overlap, indicating that the large-scale variation of the high-resolution map is well represented.

While it is common practice to deconvolve the jet width using the clean beam width, deconvolution of the surface brightness is unusual. However, for consistency this should be done, and both apparent and deconvolved surface brightness profiles are presented. The deconvolved surface brightness is shown only when the criteria described in Appendix A are satisfied.

Figures 16*a* and 16*b* show the surface brightnesses for the inner 120″ (20.5 kpc) of both jets. Knots W1–W5 and E1–E5 are indicated. Deconvolved profiles at both 3.″2 and 10.″4 resolution in the range $15'' < \Theta < 350''$ for the western and eastern jets are displayed in Figures 17*a* and 17*b*, respectively.

Both jets reach their maximum surface brightness at $\Theta \approx 35''$ (6.0 kpc); at knot W3 in the western jet and knot E4 in the eastern jet. Both jets then show a general decrease in surface brightness, interrupted only by succeeding knots, and reach approximately constant surface brightness at $\Theta \approx 110''$ (18.8 kpc). There is an enhancement in the surface brightness of the western jet at $\Theta \approx 210''$ (35.9 kpc) corresponding to the first major bend of the transverse jet oscillations.

TABLE 3

POSITIONS OF RADIO KNOTS

Knot	Θ[a]	Distance (kpc)
W0	4.″5	0.8
W1	12.4	2.1
W2	23.5	4.0
W3	33.0	5.6
W4	46.0	7.9
W5	64.0	10.9
E1	10.7	1.8
E2	18.4	3.2
E3	29.3	5.0
E4	38.8	6.6
E5	60.0	10.3

[a] Angular separation from core.

As indicated above, the I_ν-Φ relation is of great importance in an analysis of jets. For example, assuming a spectral index of $\alpha = 0.6$, a constant velocity laminar jet in a region of perpendicular magnetic field would require $I_\nu \propto \Phi^{-3.4}$. Figures 18*a*

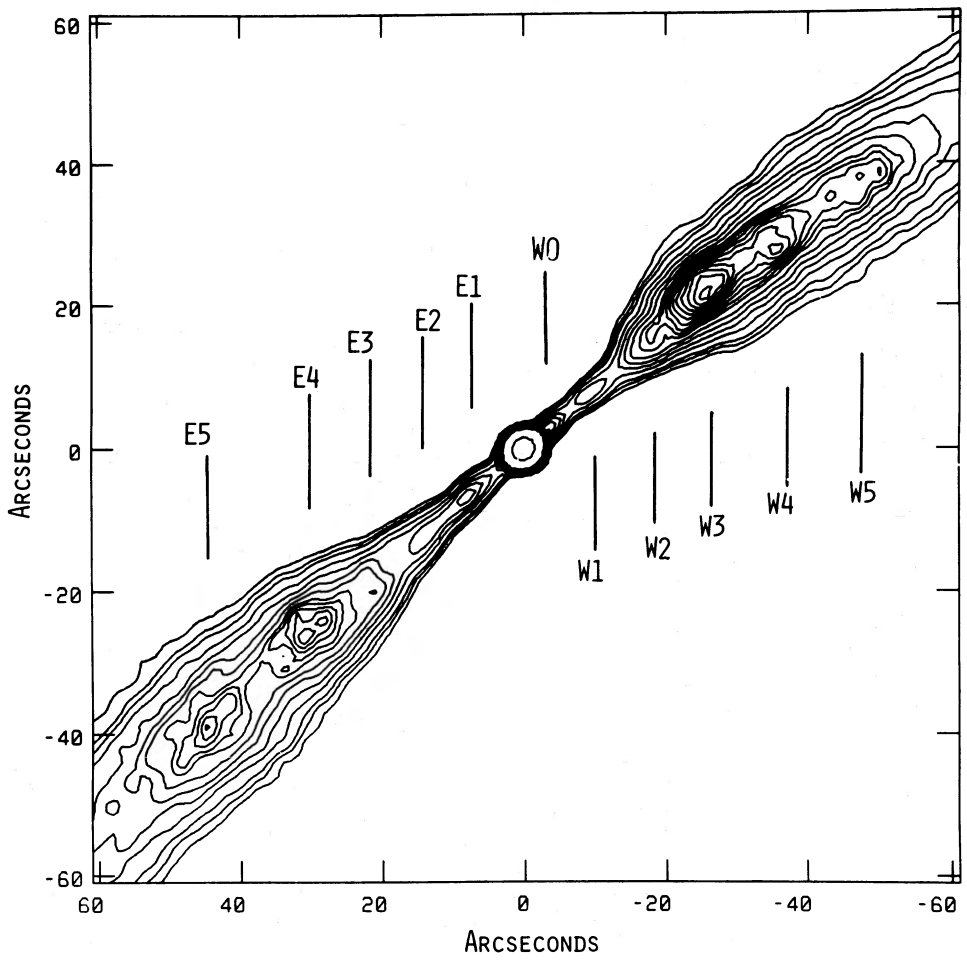

FIG. 12.—Enlargement of the central region of Fig. 10. Peak flux is 153.1 mJy per beam, and the contour levels are 1%, 1.5%, 2%, 3%, 4%, 5%, 6%, 7%, 7.5%, 8%, 8.5%, 9%, 9.5%, 10%, 10.5%, 11%, 11.5%, and 50% of the peak. Knots E1–E5 and W0–W5 are indicated, and the noise in the map is approximately 0.25 mJy per beam.

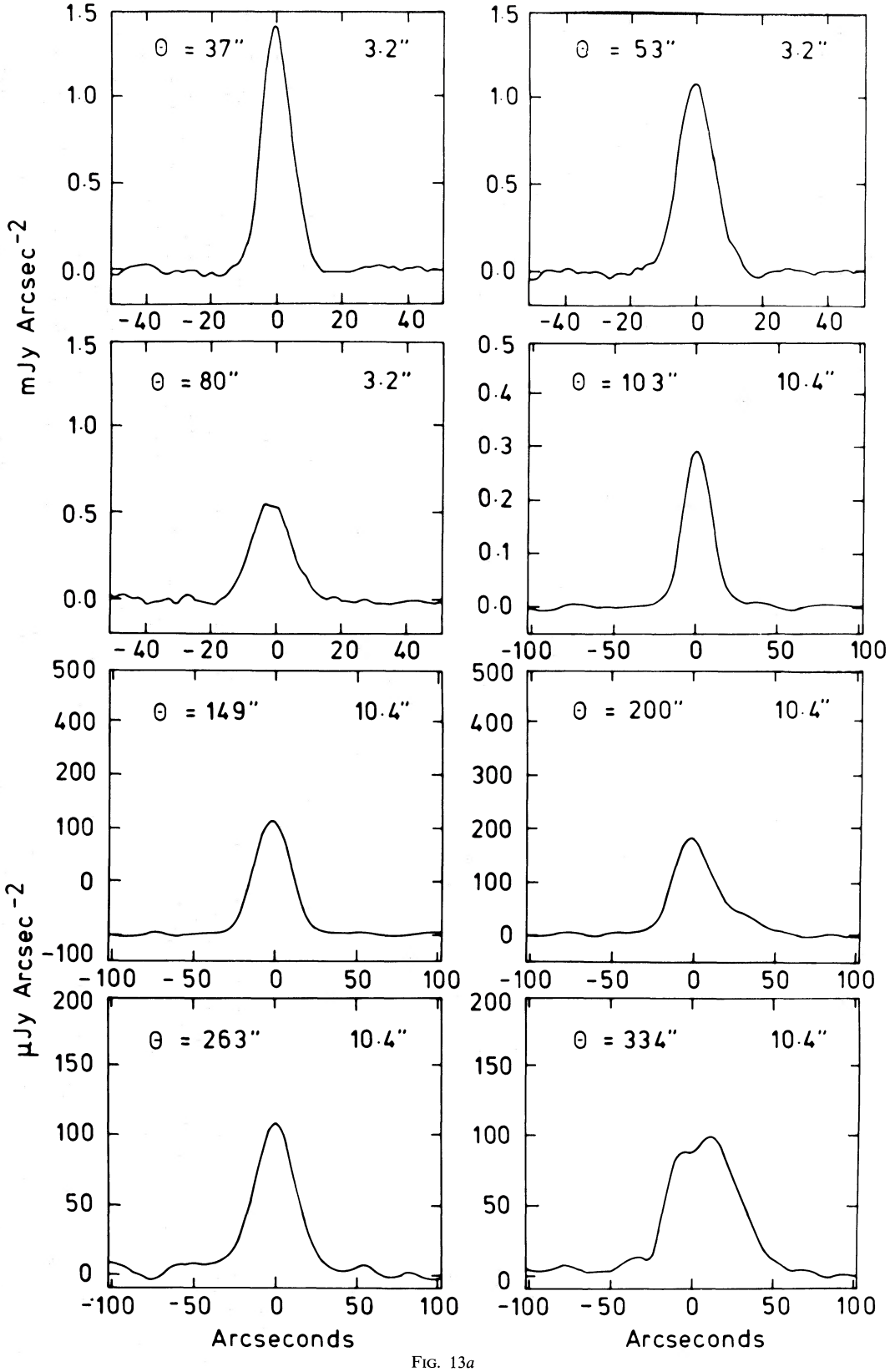

FIG. 13*a*

FIG. 13.—Some representative transverse 20 cm surface brightness profiles of the jets: (*a*) is west; (*b*) is east. The angular distance from the core, Θ (arcsec), is given in the top left corner of each panel with the resolution in the top right corner.

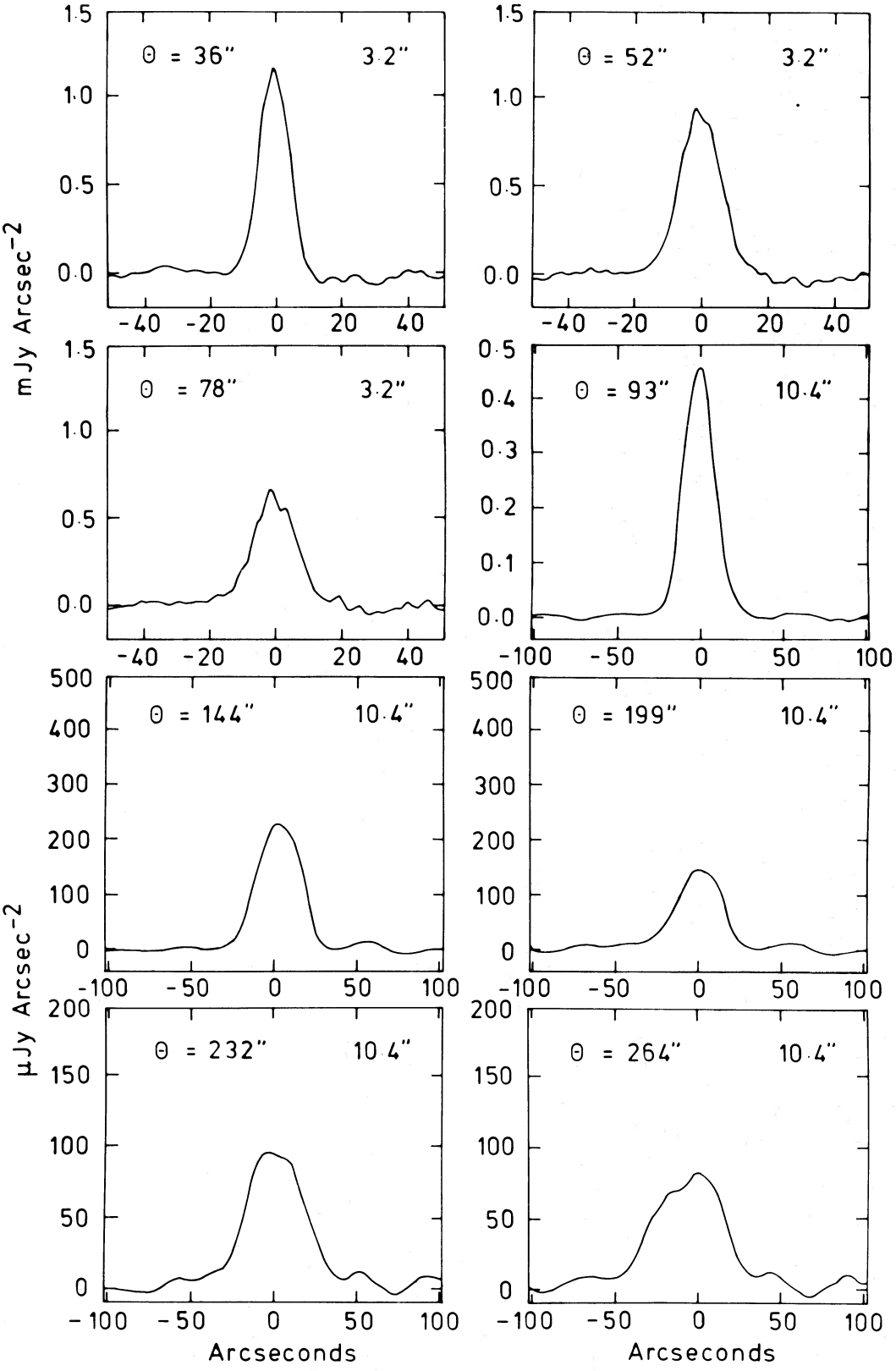

FIG. 13*b*

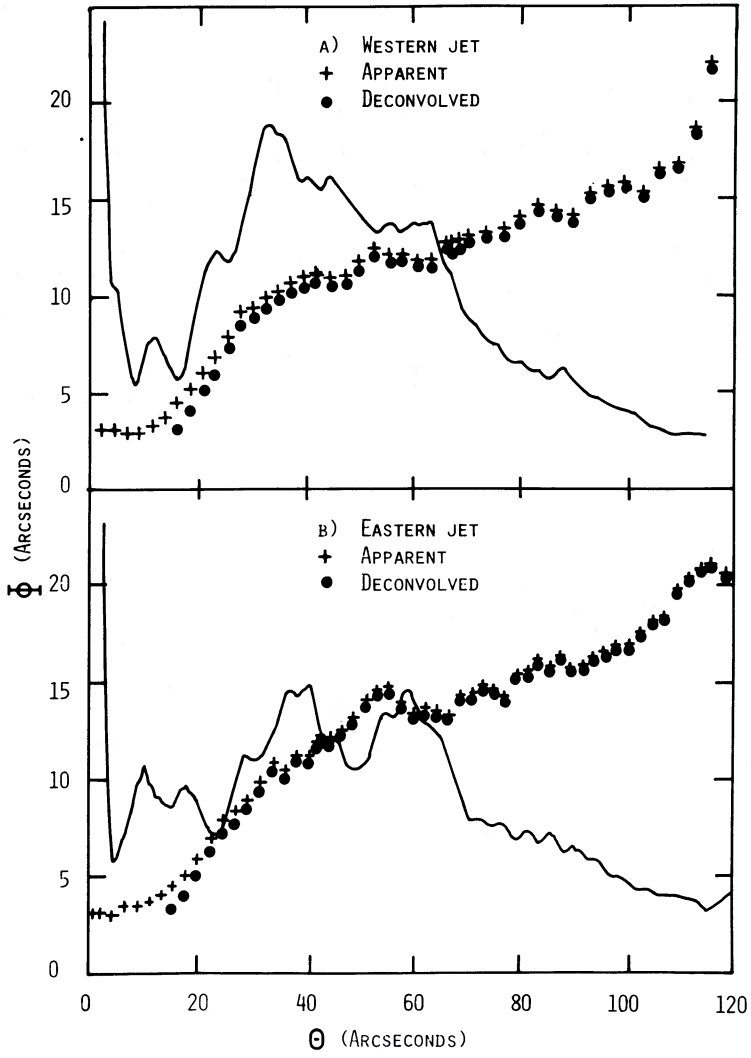

FIG. 14

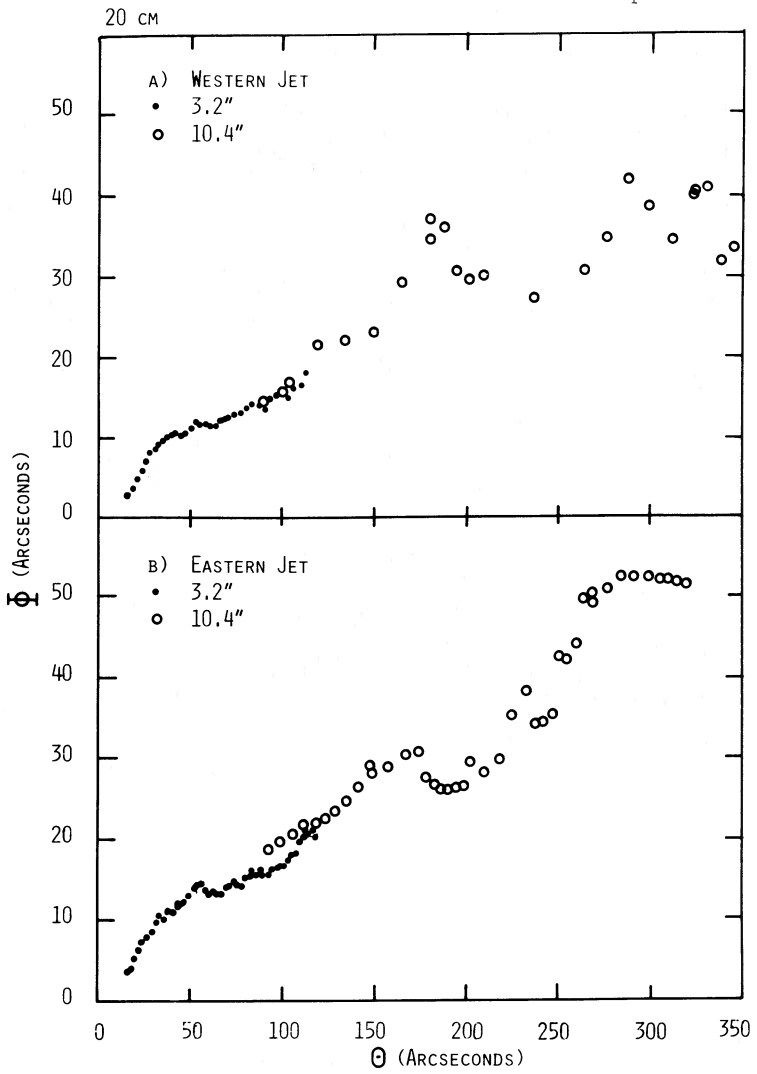

FIG. 15

FIG. 14.—Apparent and deconvolved jet FWHM, Φ (arcsec), for the inner 120″ of both jets—(*a*) is west; (*b*) is east—as a function of angular distance from the core, Θ (arcsec), at 3″.2 resolution. Superposed are the 3″.2 resolution 20 cm apparent surface brightness profiles to enable eyeball comparisons.

FIG. 15.—Deconvolved jet FWHM, Φ (arcsec), for the entirety of both jets—(*a*) is west; (*b*) is east—as a function of angular distance from the core, Θ (arcsec), at 3″.2 ($\Theta < 120''$) and 10″.4 ($\Theta > 110''$) resolution.

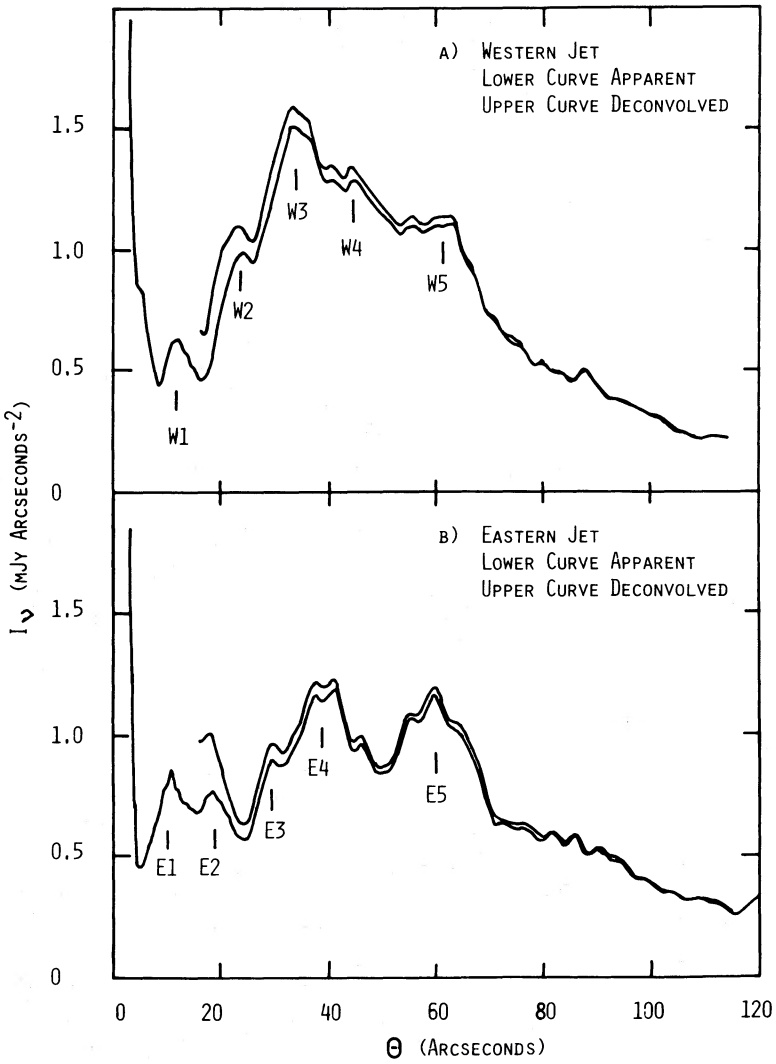

FIG. 16

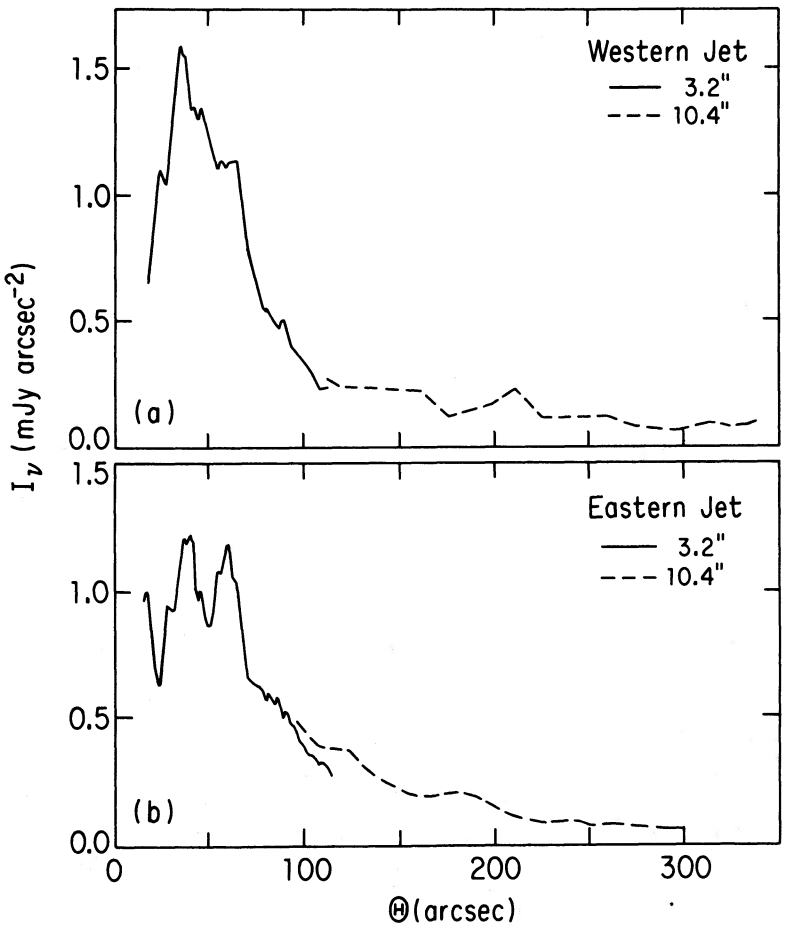

FIG. 17

FIG. 16.—Apparent and deconvolved 20 cm ridge line surface brightness, I_ν (mJy arcsec^{-2}), for the inner 120″ of both jets—(*a*) is west; (*b*) is east—as a function of angular distance from the core, Θ (arcsec), at 3″.2 resolution. Errors due to noise are approximately 0.02 mJy arcsec^{-2}.

FIG. 17.—Deconvolved 20 cm ridge line surface brightness, I_ν (mJy arcsec^{-2}), for the entirety of both jets—(*a*) is west; (*b*) is east—as a function of angular distance from the core, Θ (arcsec), at 3″.2 (Θ < 120″; errors approximately 0.02 mJy arcsec^{-2}) and 10″.4 (Θ > 120″; errors approximately 0.004 mJy arcsec^{-2}) resolution.

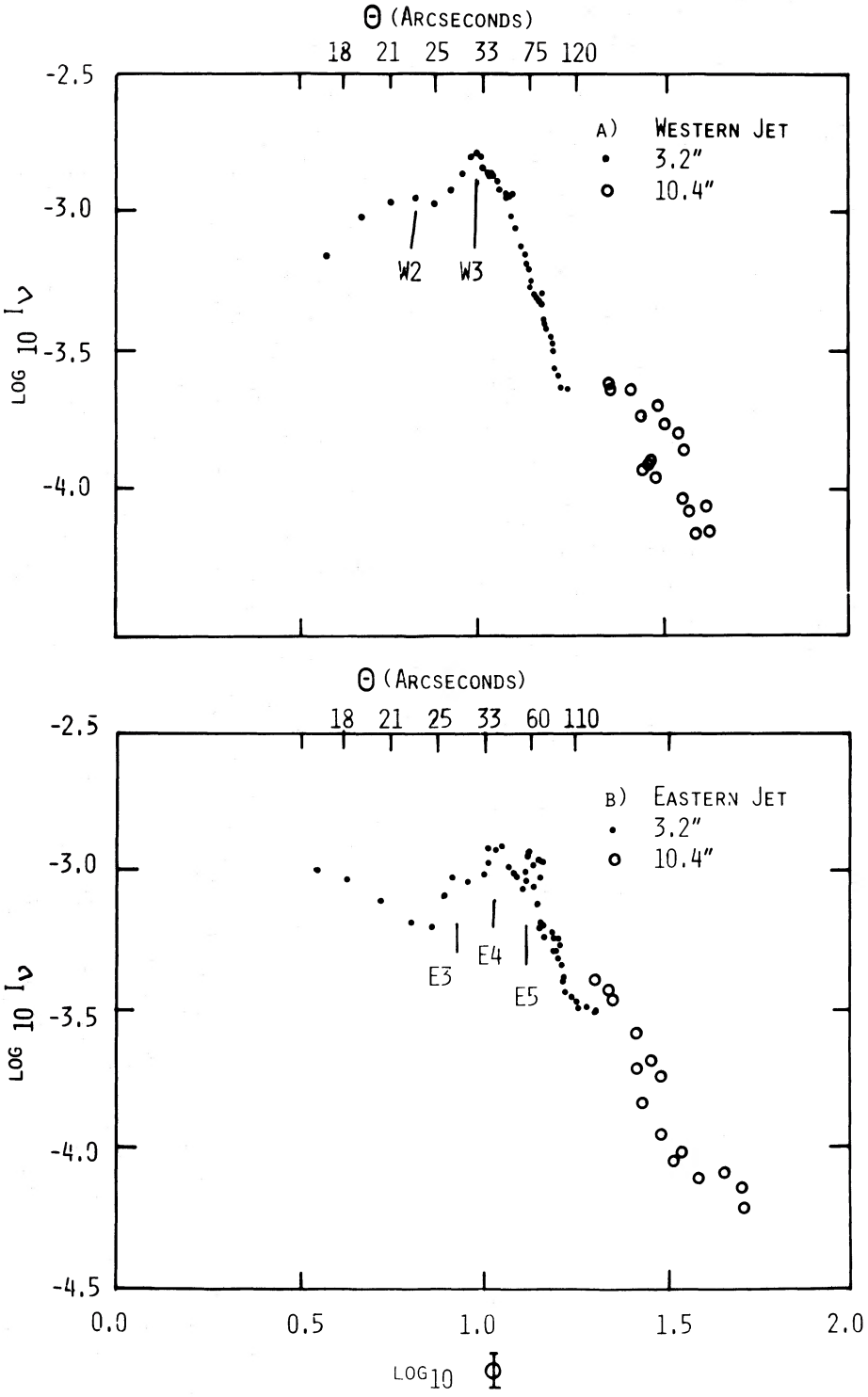

FIG. 18.—$\log_{10}$ of the deconvolved 20 cm ridge line surface brightness, I_ν (mJy arcsec^{-2}), plotted against $\log_{10}$ of the deconvolved jet FWHM, Φ (arcsec), for both jets—(*a*) is west; (*b*) is east. The 3".2 resolution data are used for $\Theta < 120''$, while for $\Theta > 120''$ the 10".4 resolution data are shown. Upper horizontal axis gives an approximate scale in Θ ($\Theta < 120''$) since Θ is generally monotonic in that region.

and 18*b* plot the 20 cm $\log_{10} I_\nu$-$\log_{10} \Phi$ relation at 3".2 and 10".4 resolution for the western and eastern jets, respectively. The higher resolution data cover the inner 120" (20.5 kpc), and the 10".4 data cover the region $120'' < \Theta < 340''$ (20.5–58.1 kpc). For the first 120", the corresponding angular distance Θ is given on the upper horizontal axis, since the Φ-Θ relation is generally monotonic for Θ in this range.

Interior to $\Theta \approx 35''$ (knot W3) I_ν increases with Φ. In the range $35'' < \Theta < 120''$ (6–20.5 kpc), I_ν varies approximately as $I_\nu \propto \Phi^{-3.8}$. In the region $110'' < \Theta < 330''$ (18.8–56.4 kpc), the relation is less well defined. This is the region in which the transverse oscillations of the jets are large with resultant oscillations in Φ.

The eastern jet follows a similar pattern. The surface brightness I_ν decreases with Φ approximately as $I_\nu \propto \Phi^{-2.9}$ from $\Theta \approx 40''$–$120''$ (6.8–20.5 kpc). However, the form of the relation is not as clear as for the western jet in the corresponding region. In the range $110'' < \Theta < 350''$, I_ν generally continues to decrease with Φ, but significant departures from a simple power law are evident.

At $\Theta \approx 320''$, the surface brightness of the eastern jet decreases more rapidly with Θ than previously. We do not have data that both adequately detect the eastern jet and transversely resolve it in this region. However, at 60" resolution, we find that $I_\nu \propto \Theta^{-1.4}$ in the range $60'' < \Theta < 330''$, whereas from $\Theta \approx 330''$–$420''$, $I_\nu \propto \Theta^{-4.5}$. For $\Theta > 420''$, the surface brightness in the eastern jet increases again, with a knot just prior to the lobe.

d) Spectral Index Distribution of the Core and Jets

It is important for spectral index determinations that flux density is not missing at either wavelength due to incomplete (u, v) coverage. Hence, we have made no attempt to evaluate the spectral index distribution in the extended lobes.

i) *The Core*

The flux densities of the core source at 1.3, 2, 6, and 20 cm are 150, 300, 224, and 153 mJy, respectively, and are plotted in Figure 19. The phase stability and dynamic range of the 1.3 cm observation are quite poor. However, after self-calibration, the jets were discernible from the core source. The flux density of the latter should be accurate to approximately 20%. To check this, observations were later made using the Parkes 64 m radio telescope at 1.3 cm, and a flux density of approximately 160 mJy was obtained for the core. Thus we are confident that the VLA 1.3 cm flux density is representative. The resultant 6–20, 2–6, and 1.3–2 cm spectral indices are $\alpha = -0.32$, -0.26, and 1.7, respectively.

ii) *The Jets*

We discuss the spectral index distribution of the jets at 3".2 resolution (6–20 cm) and 10".4 resolution (6–20 cm and 2–6 cm). Since we find no significant gradients across the jets, the data are represented by profiles along the jet ridge lines as shown in Figures 20*a* (western jet) and 20*b* (eastern jet). The bars indicate approximate errors determined from the noise in the total intensity maps. The 3".2 resolution profiles cover the inner 40" (6.8 kpc) of both jets, the 10".4 profiles reach $\Theta \approx 200''$ (34.2 kpc) for the 6–20 cm data, and the 2–6 cm spectral index is determined to $\Theta \approx 70''$ (12.0 kpc) only. The limits on Θ are set basically by the signal-to-noise ratio of the higher frequency map. As mentioned in § V*a*, the 3".2 resolution 20 cm map was made from the B + A_n data set only; this causes a slight negative bowl in the map. We estimated the depth of the bowl under each jet's ridge line from transverse surface brightness profiles. The 3".2 resolution 6–20 cm spectral index profiles were then corrected for the effect of the bowl.

First, we discuss the 6–20 cm spectral index distribution. At 10".4 resolution, the core significantly contaminates the jet spectra until $\Theta \approx 20''$ (3.4 kpc). Nevertheless, a region of steep spectral index close to the core is evident. This is most clearly seen in the 3".2 resolution profiles, where the spectral index flattens significantly from $\alpha \approx 1.0$ to $\alpha \approx 0.6$ as Θ increases from approximately 10" (1.7 kpc) to 35" (6.0 kpc). This effect is also apparent in the 10".4 profile. The effect of the negative bowl in the 3".2 map is worst in this region, but as described above, we have allowed for it. Moreover, this correction does not significantly distort the form of the spectral index profiles.

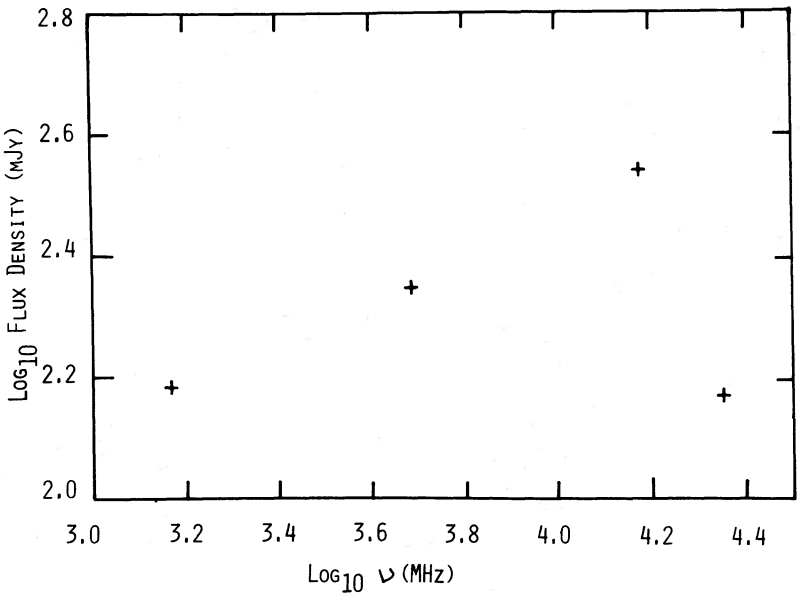

FIG. 19.—Spectrum of the unresolved core source. Resolution at each of the wavelengths 1.3, 2, 6, and 20 cm is 11", 3".5, 3".2, and 3".2, respectively.

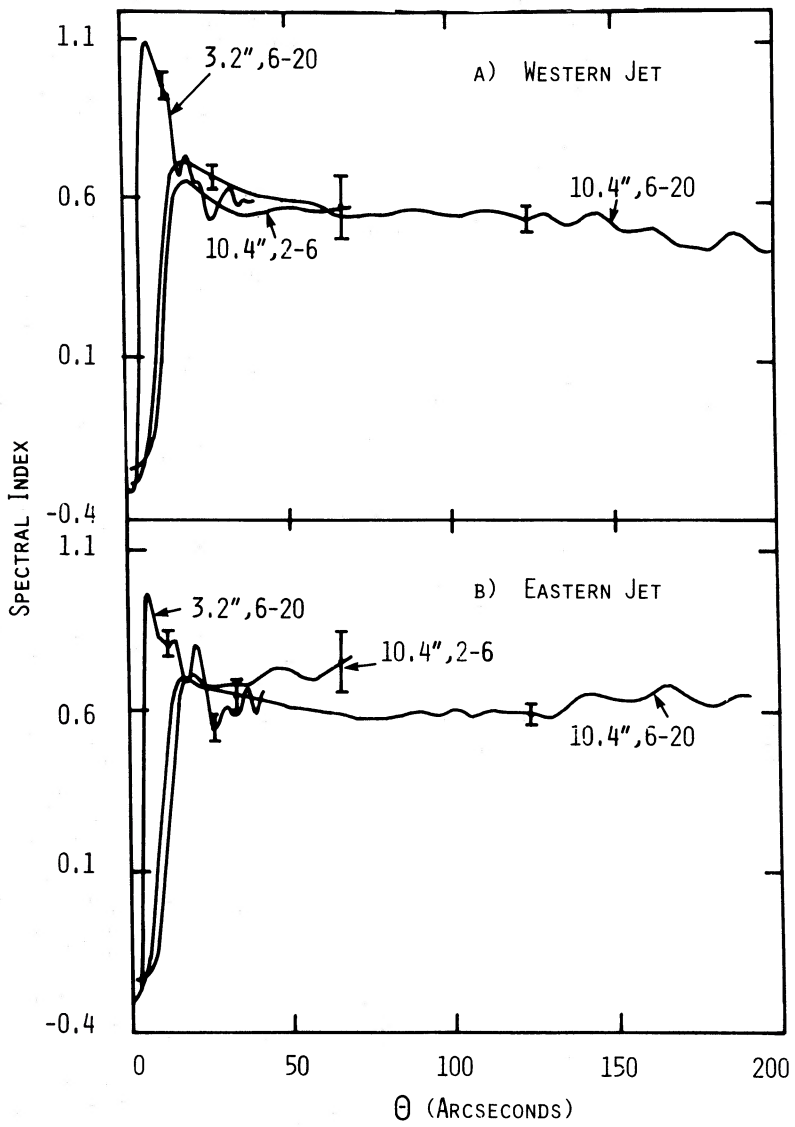

FIG. 20.—The 6–20 cm (3″.2 and 10″.4 resolution) and the 2–6 cm (10″.4 resolution) spectral index as a function of angular distance from the core, Θ (arcsec), for both jets: (*a*) is west; (*b*) is east. Bars indicate approximate errors due to noise.

The contaminating effect of the core at 10″.4 resolution also flattens the spectral index, but despite this, the profiles still steepen toward the core. Note that the 6 and 20 cm 10″.4 resolution maps were constructed from all available multi-configuration data together with zero spacing values.

Both jets show bumps in their spectral index profiles. In most cases, the bumps are such that the spectral index steepens after a knot. However, all these variations are within the expected errors in the maps, so that their reality cannot be established.

Beyond $\Theta \approx 35''$ (6.0 kpc) the spectral index of the jets flattens less rapidly, and by $\Theta \approx 60''$ (10.3 kpc) the spectral index is virtually constant at $\alpha \approx 0.63$. Note that the train of knots ceases where the spectral index becomes approximately constant in both jets.

The profiles indicate that the western jet spectral index tends to flatten as Θ increases from 100″ to 200″ (17.1–34.2 kpc); a similar steepening is observed in the eastern jet. However, there exist low-level ripples in the 10″.4 resolution 20 cm map, and their amplitude is enough to cause these effects.

We note that the bright blob in the western jet at $\Theta \approx 210''$ (35.9 kpc), corresponding to the first large bend in jet direction, is edged (on the side furthest from the nucleus) by a region of relatively flat spectral index. Typical values in the blob are $\alpha \approx 0.55$, whereas the adjoining section rapidly changes to $\alpha \approx 0.65$.

Second, we consider the 2–6 cm spectral index profiles. In the western jet we find good agreement between the 2–6 cm profile and the 3″.2 resolution 6–20 cm profile, and reasonable agreement with the 10″.4 resolution 6–20 cm profile. There are again bumps in the profiles which align with some of the knots. However, once more they are consistent with the expected errors. In the eastern jet, the 2–6 cm spectral index steepens beyond $\Theta \approx 25''$ (4.3 kpc). Although the differences (6–20 cm, 2–6 cm) are well within the errors of the data (which come mainly from the 2 cm map), the steepening is systematic. The 2 cm map is unlikely to adequately represent spatial frequencies larger than approximately 30″. However, the profile for the western jet shows no steepening over the same range in Θ, encouraging some confidence in the eastern jet 2–6 cm profile.

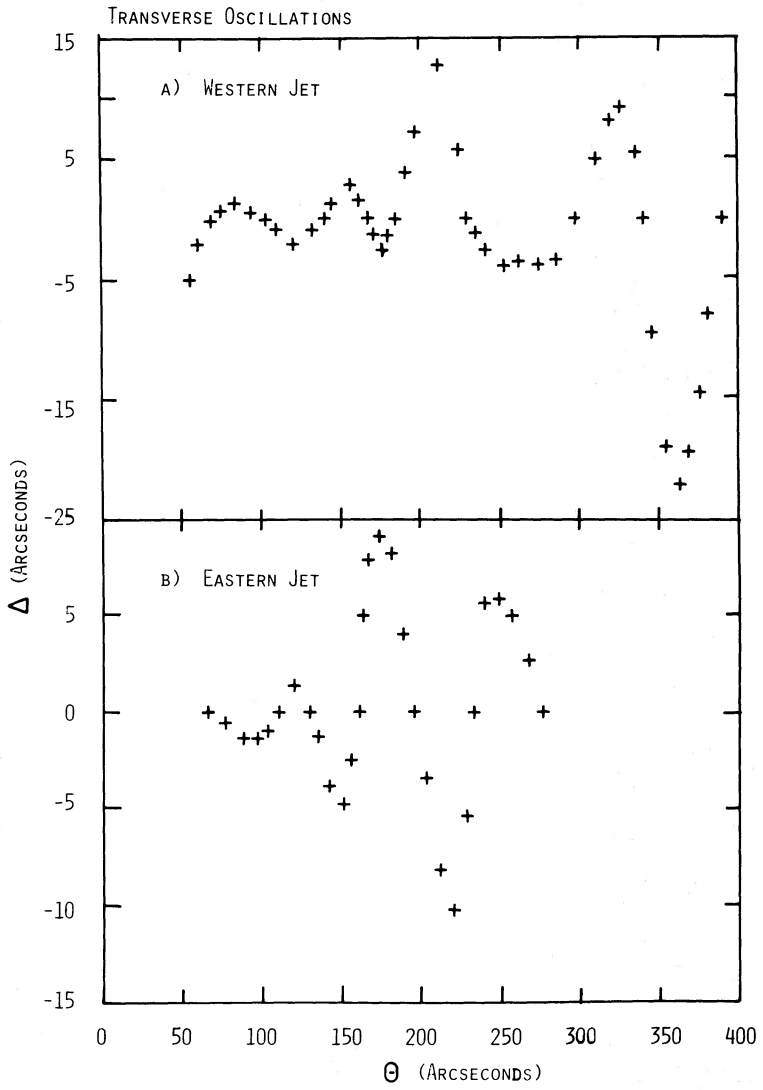

FIG. 21.—Offsets, Δ (arcsec), of both jet ridge lines—(*a*) is west; (*b*) is east—from a mean trajectory as a function of angular distance from the core, Θ (arcsec)

D-configuration observations at 2 cm are necessary to confirm this observation. There is again evidence that the spectral index flattens in both jets away from the core as the jets brighten.

e) Transverse Oscillations of the Jets

The jets show large-scale curvature and superposed smaller scale oscillations with amplitudes of the order of the jet widths. Many sources show similar oscillations, for example, 3C 449, NGC 6251, and 4C 32.69. Such oscillations may be a useful diagnostic for jets, since laboratory jets (e.g., van Dyke 1982, pp. 164, 165, or Love *et al.* 1959) show disturbances which are very similar in appearance. Offsets (Δ) of the surface brightness ridge line from mean trajectories for each jet have been measured at discrete positions along both jets using the 3.″2 (Θ < 181″) and 10.″4 (100″ < Θ < 400″) resolution maps. Figures 21*a* and 21*b* show Δ plotted against Θ for both jets with Δ positive for the ridge line north of the mean line.

The oscillations in both jets cannot be reliably measured until Θ ≈ 60″ (11.7 kpc), and the amplitude initially increases with Θ. The maximum deviation found in the western jet is Δ ≈ 22″ (3.8 kpc at Θ ≈ 360″) compared with Δ ≈ 10″ (1.7 kpc at Θ ≈ 220″) in the eastern jet. Beyond Θ ≈ 400″ (68.4 kpc), the western jet merges with the lobe, and the oscillations are more difficult to define. However, the jet can be traced into the lobe where it continues to oscillate almost until the edge of the lobe is reached (see Fig. 7). The oscillations in the eastern jet do not persist beyond Θ ≈ 275″ (47.0 kpc). This also marks the approximate region where the surface brightness declines more rapidly than previously and the jet bends northward before brightening again and entering the lobe.

Table 4 lists wavelengths (λ) derived from the extrema of the oscillations (from the mean trajectory) rather than the zeros (i.e., where the surface brightness ridge line and mean line intersect), since the mean line is to some extent arbitrary. Column (1) gives the distance from the core at which an oscillation extremum occurs. Column (2) is the distance between successive extrema, i.e., λ/2 assuming sinusoids, and column (3) is twice column (1). Column (4) gives the distance between every second extremum (the figures in parentheses indicate

TABLE 4

TRANSVERSE OSCILLATION WAVELENGTHS

Θ of Extrema (1)	λ/2 (2)	2 × (λ/2) (3)	λ (4)
Western Jet			
(1) 84″			
.....	37″	74″	
(2) 121″			70″ (1, 3)
.....	33″	66″	
(3) 154″			84″ (2, 4)
.....	51″	102″	
(4) 205″			105″ (3, 5)
.....	54″	108″	
(5) 259″			116″ (4, 6)
.....	62″	122″	
(6) 321″			100″ (5, 7)
.....	37″	74″	
(7) 358″			
Eastern Jet			
(1) 92″			
.....	26″	52″	
(2) 118″			55″ (1, 3)
.....	29″	58″	
(3) 147″			53″ (2, 4)
.....	24″	48″	
(4) 171″			71″ (3, 5)
.....	47″	94″	
(5) 218″			78″ (4, 6)
.....	31″	62″	
(6) 249″			

which extrema) i.e., λ assuming sinusoids. We note, however, that good agreement between wavelengths derived using minima and zeros was found. The wavelength range is approximately 70″–120″ (12.0–20.5 kpc) for the western jet and approximately 50″–80″ (8.6–13.7 kpc) in the eastern jet. As can be seen from Figures 21*a* and 21*b*, the oscillations in both jets are quasi-periodic until $\Theta \approx 275''$ (47.0 kpc), whereupon the dominant wavelength grows to ~110″ (18.8 kpc) in the western jet, and the eastern jet oscillations die away.

Although there are not a large number of periods in these data, a power spectrum analysis was made. This confirmed the simple measurements above; the dominant wavelengths are approximately 110″ and 70″ for the western jet and approximately 55″ and 75″ for the eastern jet.

VI. POLARIZATION DATA

a) Rotation Measure

As mentioned in § III, the effect of the ionosphere at long wavelengths can be appreciable. However, we found that the electric vector position angle maps at 20 cm made from individual observations were consistent with each other to within approximately 5°–10°. Because this indicates that the effect of the ionosphere was not large (since it is unlikely that it would be stable on a time scale of several months), we have not corrected for it.

Ideally, at least three frequencies are needed to determine unambiguously the sense of the rotation measure, and for this purpose we made observations at 2, 6, and 20 cm. Observations at 2 and 6 cm do not suffer from large ionospheric Faraday rotation. However, 2 cm position angle maps may incur errors due to uncertainties in the measurement of the position angle calibrator, and also due to poor signal-to-noise ratios in the source itself. The uncertainty in our measurement of the position angle calibrator (3C 286) was ±9° at 2 cm. Thus we cannot unambiguously determine the sense of the rotation measure from our 2, 6, and 20 cm observations alone, since there exist solutions of both signs (e.g., +60 and −30 rad m^{-2}) within the errors of the 2 cm observation. However, Gardner and Davies (1964) have obtained low-resolution polarization data using the Parkes 64 m radio telescope at 6, 11, 21, 30, and 31 cm, providing an average position angle for each lobe and the jets as a whole. They found a rotation measure of −34 rad m^{-2}, in excellent agreement with one of our solutions. This is also the correct sense of rotation as determined by Simard-Normandin, Kronberg, and Button (1981) for sources in nearby regions of the sky. Therefore, we evaluated the rotation measure from the 6 and 20 cm data only, and constrained the solution to be consistent with the results of Gardner and Davies (1964).

We have determined the rotation measure in the jets at 3.″2 and 10.″4 resolution. All significant rotation measures are in the range −40 to 0 rad m^{-2} at both resolutions, with most variation between −30 and −20 rad m^{-2}. In general, the rotation measures associated with the eastern jet are slightly higher than those found for the western jet. The errors due to noise in the initial Stokes Q and U maps are never more than 0.5 rad m^{-2} and better than 0.1 rad m^{-2} where the jets are brightest. Figure 22 shows a contour map of −1 times the rotation measure distribution at 10.″4 resolution. Both jets show pockets and small transverse gradients of the order of 15 rad m^{-2}, but no systematic large-scale trends or rapid changes in rotation measure are present. The rotation measure distribution at 3.″2 resolution reveals no additional structure and is not presented here.

Rotation maps of the lobes as well as the jets have been made. The 6 cm data were heavily tapered to produce 60″ resolution maps which, in conjunction with the equivalent resolution 20 cm map, enabled low-resolution rotation measures of the lobes to be found. Once again, all rotation measures are between −10 and −40 rad m^{-2} with no apparent systematic trends.

b) Orientation of the Magnetic Field

With the use of the rotation measure distribution described above, we produced position angle maps of the electric vectors at zero wavelength. A further rotation of 90° was then added to give the projected direction of the dominant magnetic field component. The estimated errors due to noise are everywhere less than 10°, and on the order of 1° where the jets are brightest.

Figure 23 displays the projected magnetic field at 10.″4 resolution overlaid on 20 cm total intensity contours. A striking degree of uniformity in the magnetic field is evident from these maps. A change in the position angle of the projected magnetic field from longitudinal to transverse occurs in both jets between the core and where the jets rapidly brighten or "turn on." This is shown more clearly by slice plots of the position angle of the magnetic field along the western and eastern jets in Figures 24*a* and 24*b*, respectively. As the jets begin to oscillate, the projected magnetic field generally remains perpendicular to the surface brightness ridge lines. There are, however, areas at some of the oscillation extrema where the projected magnetic field vectors at the jet edges

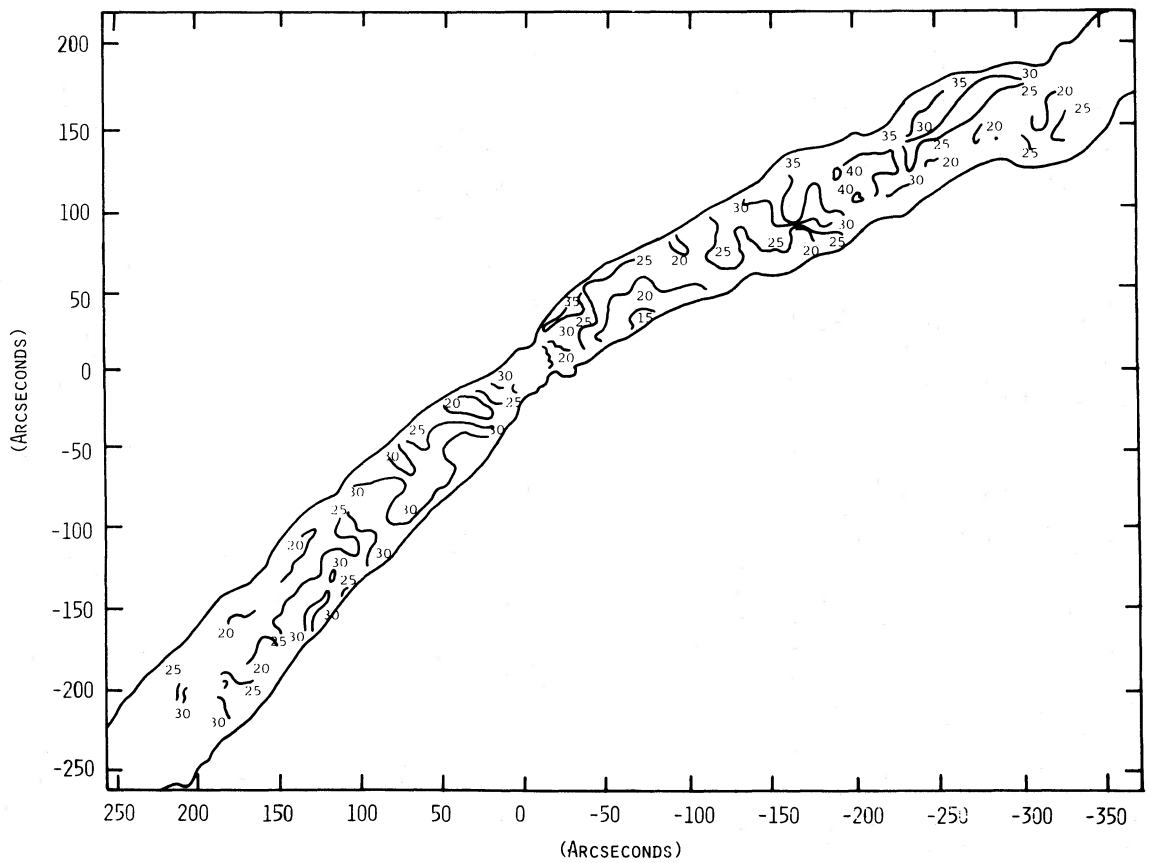

FIG. 22.—Schematic contour diagram of -1 times the 6–20 cm rotation measure (rad m^{-2}) at 10.″4 resolution. Outer contour is at the total intensity, 20 cm, 10.″4 resolution, 1% of peak level (see Fig. 8).

become longitudinal, while they remain transverse at the jet centers.

The higher resolution (3.″2) data shown in Figures 25*a* and 25*b* are similar. The projected magnetic field in both jets is dominated by the longitudinal component until $\Theta \approx 18''$ (3.1 kpc), whereupon it rapidly changes to a transverse dominant state (Figs. 24*a* and 24*b*). This transition is accompanied by the rapid expansion of the jets (see § V*b*). Just beyond the polarization minimum (see § VI*c*) the projected magnetic field becomes transverse at the jet center, but remains longitudinal at the jet edges. The estimated errors are not large enough to cause the observed transverse variations in the projected magnetic field position angle profiles either as the jets are flaring or where the jets oscillations are large.

Figures 26*a* and 26*b* show the projected magnetic field for the western and eastern lobes overlaid on 20 cm contours. Good alignment of the magnetic field vectors with the outer contours of the lobes is evident. There are a few vectors throughout Figure 26*b* that are atypical and disordered when compared with the surrounding vectors. The unrotated vectors, however, are well ordered. Given the general uniformity in the rotation measure of this source, it is most likely that these regions are due to noise in the 6 cm position angle map.

c) Degree of Polarization

The degree of polarization $P = (Q^2 + U^2)^{1/2}/I$ has been determined at 3.″2 (6 and 20 cm), 10.″4 (2, 6, and 20 cm), and 60″ (20 cm) resolution. The lengths of the vectors in Figures 23, 25, and 26 represent the degree of polarization at 20 cm.

The degree of polarization was estimated from the observed polarization using the maximum likelihood estimate in Appendix B. This estimate differs most from the observed polarization at low signal-to-noise ratios and agrees with the estimate of Wardle and Kronberg (1974) at high signal-to-noise ratios.

Both extended lobes are polarized, with values ranging from $P \approx 10\%$–40% (see Figs. 26*a* and 26*b*) at 60″ resolution. The eastern lobe is, in general, more highly and uniformly polarized than its western counterpart, with P typically between 20% and 40% compared with 10%–15%. The western lobe, however, does show significant enhancement at the outer edge, where P rises to between 25% and 35%.

None of our data exhibits significant trends transverse to the jets. Therefore, 10.″4 and 3.″2 resolution slice plots of the degree of polarization along both jet ridge lines are given in Figures 27*a* and 27*b*. Note, however, that the 10.″4 resolution slice plots are derived from the 6 cm map, whereas the 3.″2 resolution slices are from the 20 cm map. The reason for this is as follows. The 20 cm 10.″4 resolution map was made from a concatenated data base. As mentioned in § VI*a*, the agreement between the individual data base position angle maps was better than 10°. Although this is good agreement (at least for a low declination source), there is still a loss of polarized intensity because of the vector averaging of the individual data bases. A comparison of the 6 and 20 cm 10.″4 resolution slice plots does indeed show a small (less than 10%) systematic difference in

polarization between the two wavelengths. The 6 cm map is therefore used to display the degree of polarization at 10″.4 resolution. The 3″.2 resolution 20 cm map was produced from a single observation and therefore does not suffer from the above problem. It is used in preference to the equivalent resolution 6 cm data to display the degree of polarization in the inner parts of the jets because of its superior signal-to-noise ratio. Small oscillations of the order of 4% in the 3″.2 resolution slice plots are noise. Local values of up to 60% should also be attributed to noise, since a detailed examination of the data indicates that these are atypical compared with the local surrounding values.

The mean behavior of the polarization is exhibited by the 10″.4 data. At this resolution, values of $P \approx 10\%$ at both jet bases increase smoothly to maxima of $P \approx 40\%$ in the western jet and $P \approx 45\%$ in the eastern jet (at $\Theta \approx 60''$, 10.3 kpc). These maxima correspond to the regions immediately following knots W5 and E5 where the surface brightness begins to decrease rapidly. In general, the eastern jet is slightly more highly polarized than the western jet, and P varies between 40% and 45% (for the region $60'' \lesssim \Theta \lesssim 120''$) compared with 35%–40% for the western jet. Beyond $\Theta \approx 120''$ (20.5 kpc), both jets show oscillations of P ranging from 10% to 40%, coinciding with the transverse oscillations of the jets.

From the 3″.2 resolution slice plots we see details in the region close to the core. In the western jet there are peaks where $P \approx 20\%$ at $\Theta \approx 7''$ and 15″ (1.2 and 2.6 kpc). The first corresponds to the knot W0, and the second is slightly after the peak of knot W1. Similarly, P rises to approximately 15% at $\Theta \approx 12''$ (2.1 kpc) in the eastern jet at knot E1. However, knot E2 does not show any significant polarization since it corresponds to the point where the projected magnetic field changes orientation (see below).

There exist polarization minima that correspond to the rapid change in position angle of the projected magnetic field vectors (see § VI*b*) at $\Theta \approx 18''$ (3.1 kpc) in both jets. These minima are in the region of rapidly increasing jet widths. Beam smearing of the polarized emission in a region of rapidly changing field position angle will contribute to such minima. However, beyond the minima the degree of polarization rises smoothly (in a region of uniform projected magnetic field) to its maximum over approximately 15 beams. Thus, low values of P nearby to the minima must be low for reasons other than beam smearing, and presumably reflect the intrinsic magnetic field geometry.

A comparison between 2 and 6 cm (10″.4 resolution) and 6 and 20 cm (3″.2 and 10″.4 resolution) of the degree of polarization shows no evidence for depolarization. However, we note that the 20–6 cm depolarization ratio (P_{20}/P_6) is systematically approximately 0.9 over both jets at 10″.4 resolution. This is probably a result of the vector averaging of the constituent data bases at 20 cm and the resultant loss of polarized intensity described above. It is consistent with the 10° variation of

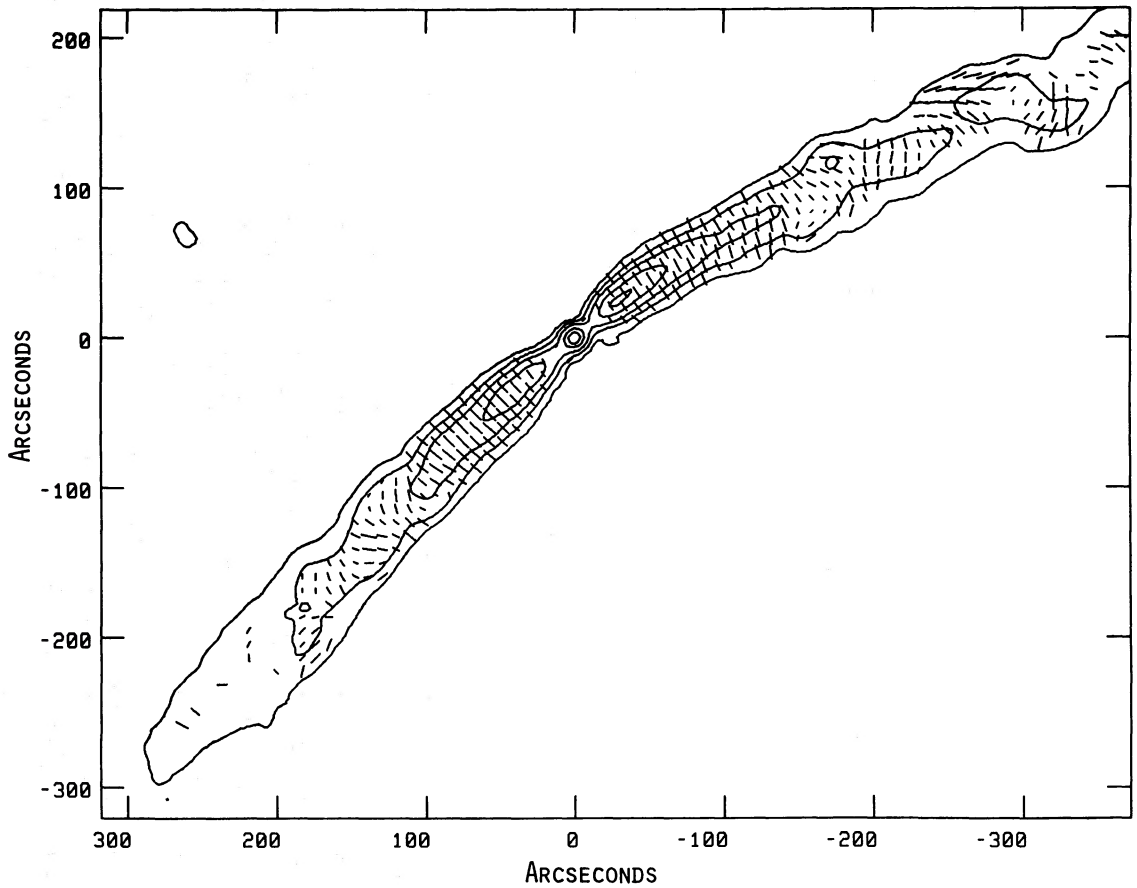

FIG. 23.—Simplified 20 cm 10″.4 resolution total intensity contours of the jets with superposed degree of polarization vectors at the projected magnetic field position angle. Peak flux is 163.1 mJy per beam, and the contour levels are 1%, 5%, 15%, 40%, and 70% of the peak. Vector of length 1″ represents 3.8% degree of polarization.

polarization position angles in the constituent data bases. The 6–2 cm depolarization ratio is statistically consistent with 1.0.

VII. MINIMUM ENERGY DENSITY AND PRESSURE

Equipartition conditions are unlikely to be satisfied along the entire length of a jet. However, minimum energy estimates of particle energy densities and magnetic field strengths are probably indicative, and are useful in determining the minimum pressure required of a confining atmosphere. We have calculated the minimum energy density in particles and fields ($\epsilon_t^{\min \epsilon}$), the corresponding magnetic field ($B^{\min \epsilon}$), and the minimum total pressure ($P_t^{\min P}$). The transverse surface brightness profiles of the jets in PKS 1333−33 are well described by Gaussians. Therefore, we have calculated the equipartition parameters for Gaussian profile jets using the formulae derived in Appendices C and D. We have used the standard formulae (e.g., Pacholczky 1970) for the lobes. The following assumptions have been made:

1. Since the jets of PKS 1333−33 are at the upper end of the range of projected jet lengths (Bridle and Perley 1984), it is reasonable to assume that they are perpendicular to the line of sight.

2. The angle between the line of sight and the magnetic field direction is 90°. The projected field is transverse in the region for which we calculate the equipartition parameters, so this may be a reasonable assumption.

3. Equal energies are assigned to the relativistic electron and relativistic proton plus thermal particle distributions. This is yet to be observationally or theoretically justified.

4. The jet spectra are power laws (as is commonly observed in a limited range) extending from a lower cutoff frequency at 10 MHz to an upper cutoff at 100 GHz. The same lower cutoff, but an upper cutoff of 10 GHz, was assumed for the lobes. It should be noted that the dependence on the upper cutoff is weak. The lower cutoff is largely chosen for comparison with other sources.

5. The spectral index $\alpha = 0.63$ ($S_\nu \propto \nu^{-\alpha}$) for both jets (the regions of steep spectral index in both jets are interior to the minimum Θ used for these calculations), and $\alpha = 0.6$ for each lobe.

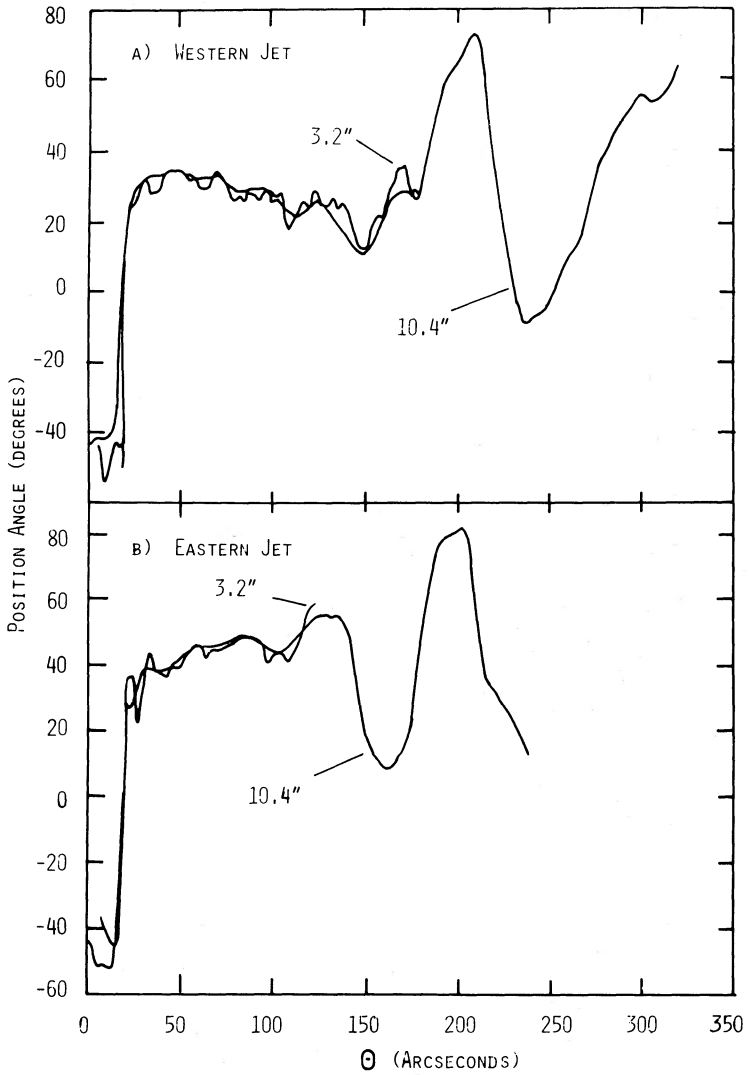

FIG. 24.—Position angle of the projected magnetic field at 3.″2 and 10.″4 resolution for both jets—(*a*) is west; (*b*) is east—as a function of angular distance from the core, Θ (arcsec).

TABLE 5

SYNCHROTRON PARAMETERS

L (ergs s^{-1})	$\epsilon_t^{\min \epsilon}$ (ergs cm^{-3})	$B^{\min \epsilon}$ (G)	$P_t^{\min P}$ (dyne cm^{-2})	
1.5×10^{41}.....	...	...	...	total source
5.9×10^{40}.....	4.1×10^{-13}	2.1×10^{-6}	2.2×10^{-13}	western lobe
3.5×10^{40}.....	2.1×10^{-13}	1.5×10^{-6}	1.1×10^{-13}	eastern lobe

6. The filling factor is unity.

The energy densities and magnetic field strengths are plotted in Figures 28 and 29, respectively. The small-scale structure reflects the surface brightness profiles. The values are derived from the 3.″2 resolution data to $\Theta \approx 120''$ (20.5 kpc) and the 10.″4 resolution data from $\Theta \approx 120''$ (26.5 kpc). Typical energy densities range from 3×10^{-11} ergs cm^{-3} ($P_t^{\min P} = 1.5 \times 10^{-11}$ dyne cm^{-2}) as the jets are flaring, to approximately 2×10^{-12} ergs cm^{-3} ($P_t^{\min P} = 1 \times 10^{-12}$ dyne cm^{-2}) at large Θ. The minimum energy magnetic field has a similar form, decreasing from approximately 20 μG to 5 μG over a similar range in Θ.

Although our data would be unreliable in the determination of spectral indices for the lobes, the integrated 20 cm flux densities are unlikely to be significantly in error. For the western lobe, we find $\epsilon_t^{\min \epsilon} = 4.1 \times 10^{-13}$ ergs cm^{-3} ($P_t^{\min P} = 2.2 \times 10^{-13}$ dyne cm^{-2}) and $B^{\min \epsilon} = 2.1$ μG. Similarly, for the eastern lobe, $\epsilon_t^{\min \epsilon} = 2.1 \times 10^{-13}$ ergs cm^{-3} ($P_t^{\min P} = 1.1 \times 10^{-13}$ dyne cm^{-2}), and $B^{\min \epsilon} = 1.5$ μG. The luminosities and equipartition parameters for the overall source and the lobes individually are summarized in Table 5.

VIII. SUMMARY

In this paper we have presented multifrequency VLA observations of the radio galaxy PKS 1333−33. The main features of these observations are the following:

1. Two symmetric, slightly curved jets issue from an unresolved core and terminate in mildly edge-brightened lobes. The

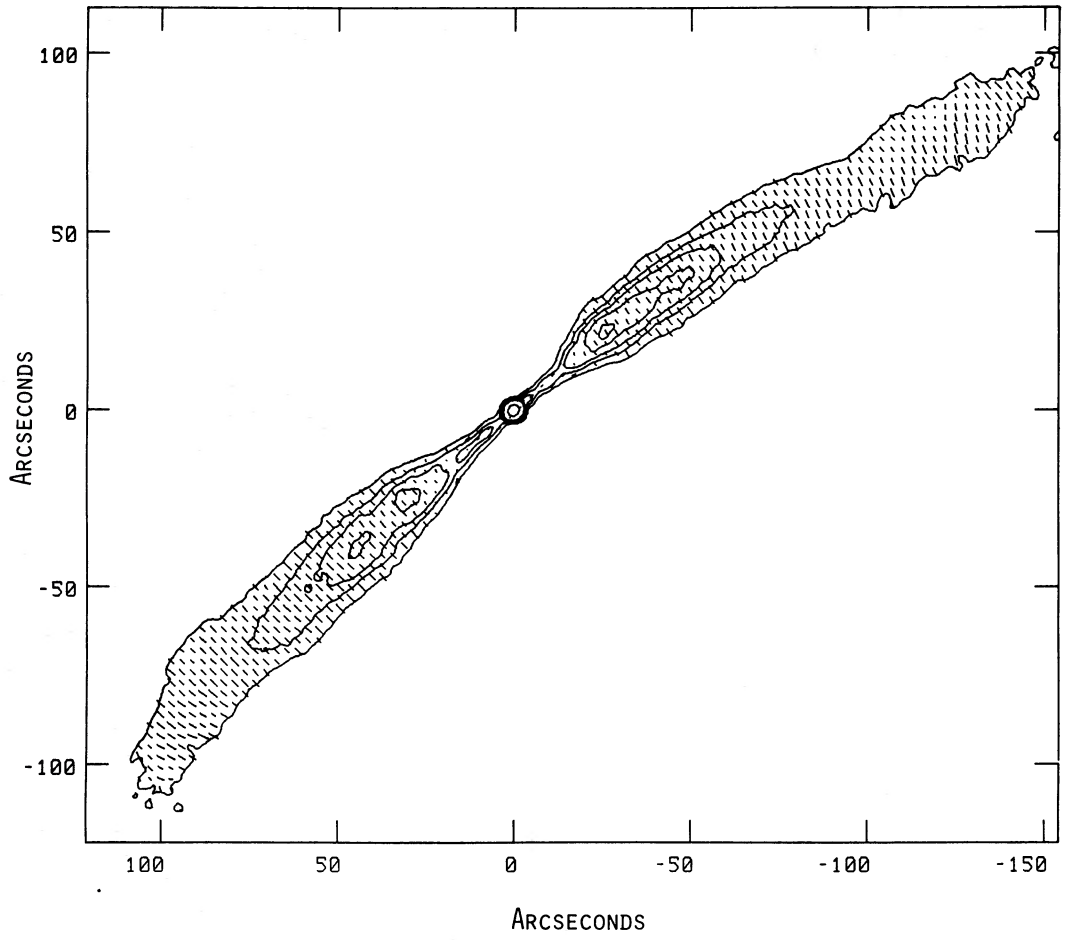

FIG. 25a

FIG. 25.—(*a*) Simplified 20 cm 3.″2 resolution total intensity contours of the jets with superposed 20 cm degree of polarization vectors at the projected magnetic field position angle. Peak flux is 153.1 mJy per beam, and the contour levels are 1%, 3%, 5%, 8%, 11%, and 50% of the peak. Vector of length 1″ represents 18.9% degree of polarization. (*b*) Enlargement of the central region of (*a*). Peak flux is 153.1 mJy per beam, and the contour levels are 1%, 3%, 4%, 5%, 7%, 9%, 11%, and 50% of the peak. Vector of length 1″ represents 22.1% degree of polarization.

overall projected extent of the source is approximately 35′ (360 kpc); the projected distance of the western lobe from the core is approximately 130 kpc compared with approximately 190 kpc for the eastern lobe.

2. The jets are initially unresolved (at 3″.2 resolution) before flaring rapidly ($d\Phi/d\Theta \approx 0.45$) at $\Theta \approx 15''$ (2.6 kpc). The rate of expansion then slows to $d\Phi/d\Theta \approx 0.1$ at $\Theta \approx 35''$ (6.0 kpc) in both jets.

3. Transverse oscillations of both jets are recognizable beyond $\Theta \approx 60''$ (10.3 kpc), with wavelengths ranging from 70″ to 120″ in the western jet and 50″ to 80″ in the eastern jet. The western jet and its accompanying oscillations can be observed throughout the western lobe, almost until the outer edge is reached. However, the oscillations do not persist beyond $\Theta \approx 275''$ (47.0 kpc) for the eastern jet.

4. A train of knots in both jets occurs in the approximate range $5'' < \Theta < 60''$ (0.9–10.3 kpc). At 3″.2 resolution, I_ν varies between the surface brightness peaks (knots W3 and E4) and the regions of large transverse oscillation as $I_\nu \propto \Phi^{-3.8}$ and $I_\nu \propto \Phi^{-2.9}$ in the western and eastern jets, respectively. In the regions between the core and the surface brightness peaks, and in the regions of strong transverse oscillation there are no well-defined relations between I_ν and Φ in either jet.

5. The unresolved central core has 6–20 cm, 2–6 cm, and 1.3–2 cm spectral indices ($S_\nu \propto \nu^{-\alpha}$) of $\alpha = -0.32$, -0.26, and 1.7, respectively. On either side of the core, the unresolved jets show a steep spectral index ($\alpha \approx 1$) which flattens as Θ increases and approaches the mean jet value of $\alpha = 0.63$ by $\Theta \approx 35''$ (6.0 kpc). The spectral index flattens less rapidly until $\Theta \approx 60''$ where it becomes approximately constant. This also marks the termination of the train of knots. There are no significant gradients in spectral index transverse to the jets.

6. All rotation measures are between -40 and 0 rad m^{-2} and typically between -30 and -20 rad m^{-2}, with no systematic or large gradients.

7. The projected magnetic field shows two distinct orientations. The longitudinal component dominates interior to $\Theta \approx 18''$ (3.1 kpc), whereupon the transverse component dominates. There is some evidence that the projected magnetic field is longitudinal at the jet edges and transverse at the jet centers in the region where the jets flare rapidly, close to the core. Similar behavior in the projected magnetic field is also seen at some of the extrema of the later jet oscillations. The projected magnetic field is well aligned with the total intensity contours at the outer edges of both lobes.

8. The degree of polarization varies from approximately 5% to 45% in both jets, with the eastern jet generally slightly more highly polarized than the western jet. The degree of polarization is minimum where the magnetic field changes from longitudinal to transverse and then increases smoothly to values of ~35%–45% by $\Theta \approx 60''$ (10.3 kpc). Beyond $\Theta \approx 120''$ (20.5 kpc), there are large oscillations in the degree of polarization as the jets oscillate. There is no evidence for depolarization in the jets. Both lobes show degrees of polarization from 10% to

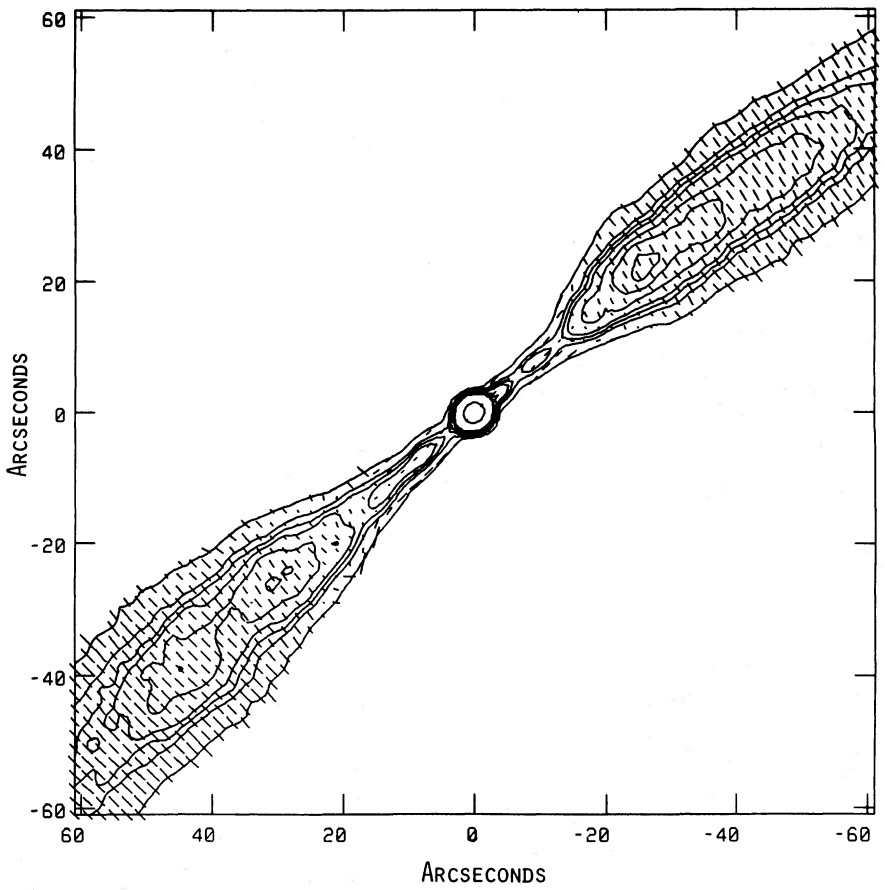

FIG. 25*b*

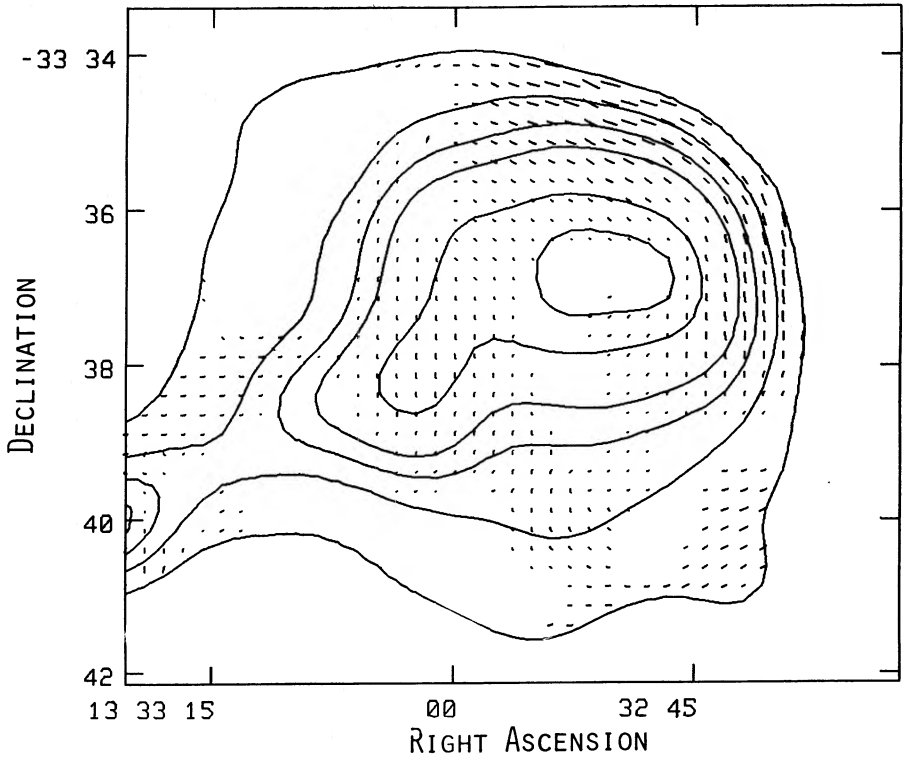

FIG. 26*a*

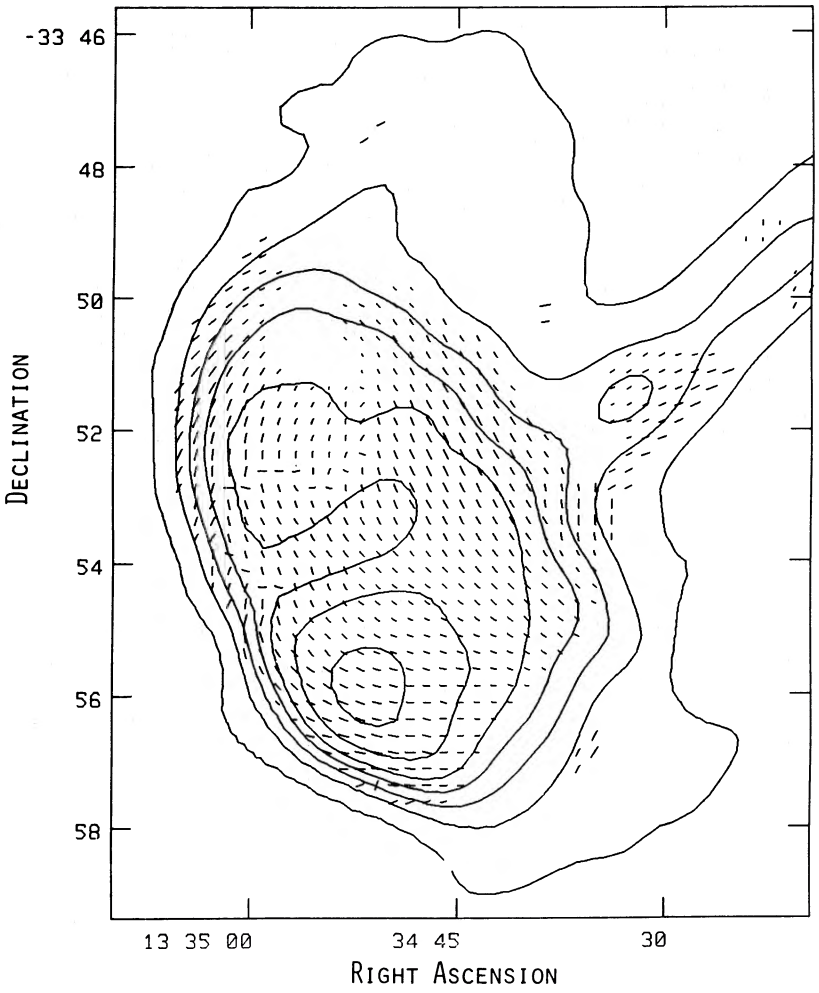

FIG. 26*b*

FIG. 26.—(*a*) Simplified 20 cm 60″ resolution total intensity contours of the western lobe with superposed 20 cm degree of polarization vectors at the projected magnetic field position angle. Peak flux is 748.3 mJy per beam (not visible on this diagram), and the contour levels are 5%, 10%, 15%, 20%, 30%, and 35% of the peak. Vector of length 1″ represents 3.5% degree of polarization. (*b*) Simplified 20 cm 60″ resolution total intensity contours of the eastern lobe with superposed 20 cm degree of polarization vectors at the projected magnetic field position angle. Peak flux is 745.8 mJy per beam (not visible on this diagram), and the contour levels are 1.5%, 4%, 6%, 8%, 10%, 13%, and 17% of the peak. Vector of length 1″ represents 3.4% degree of polarization.

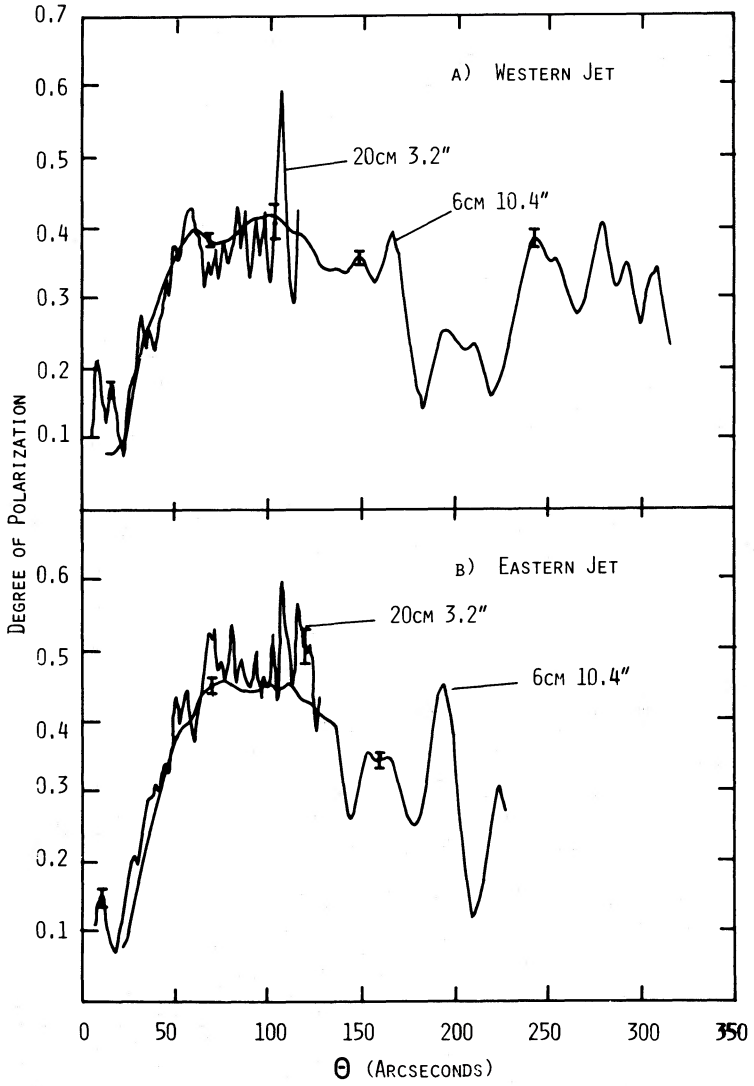

FIG. 27

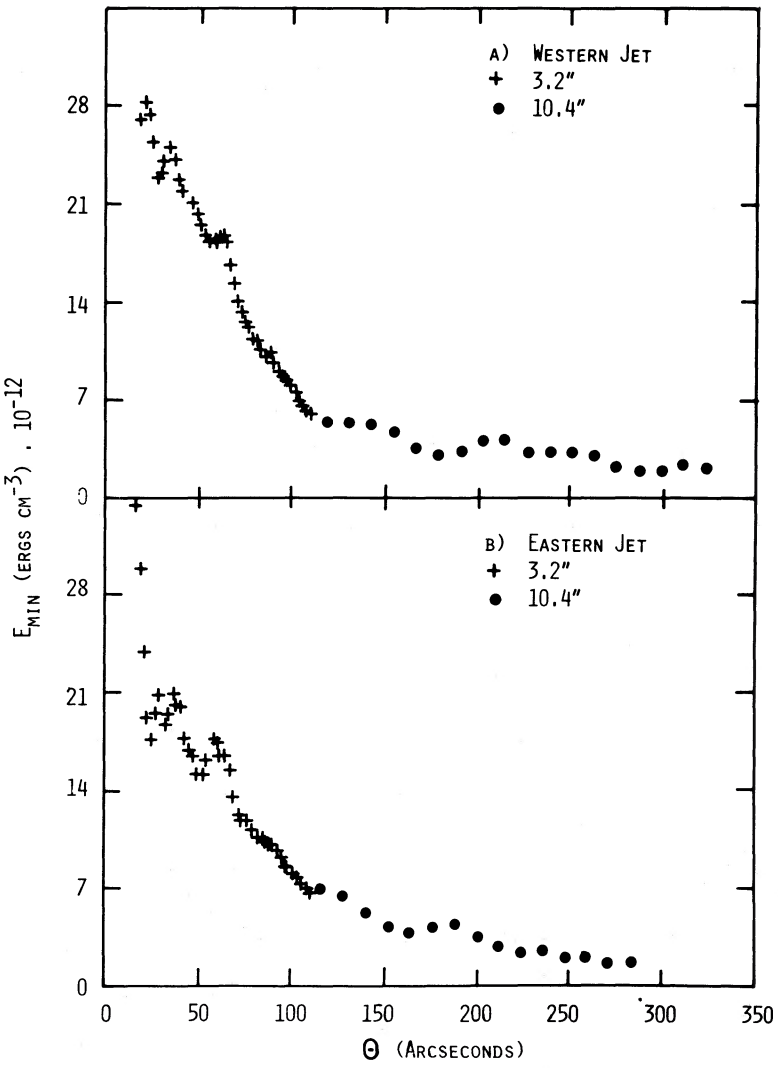

FIG. 28

FIG. 27.—Degree of polarization along the ridge lines of both jets—(*a*) is west; (*b*) is east—at 10.″4 (6 cm) and 3.″2 (20 cm) resolution as a function of the angular distance from the core, Θ (arcsec). Bars indicate approximate errors due to noise.

FIG. 28.—Minimum energy density (particles and fields) along both jets: (*a*) is west; (*b*) is east. The 3.″2 resolution 20 cm map is used until $\Theta \approx 100''$, whereupon the 10.″4 resolution map is used.

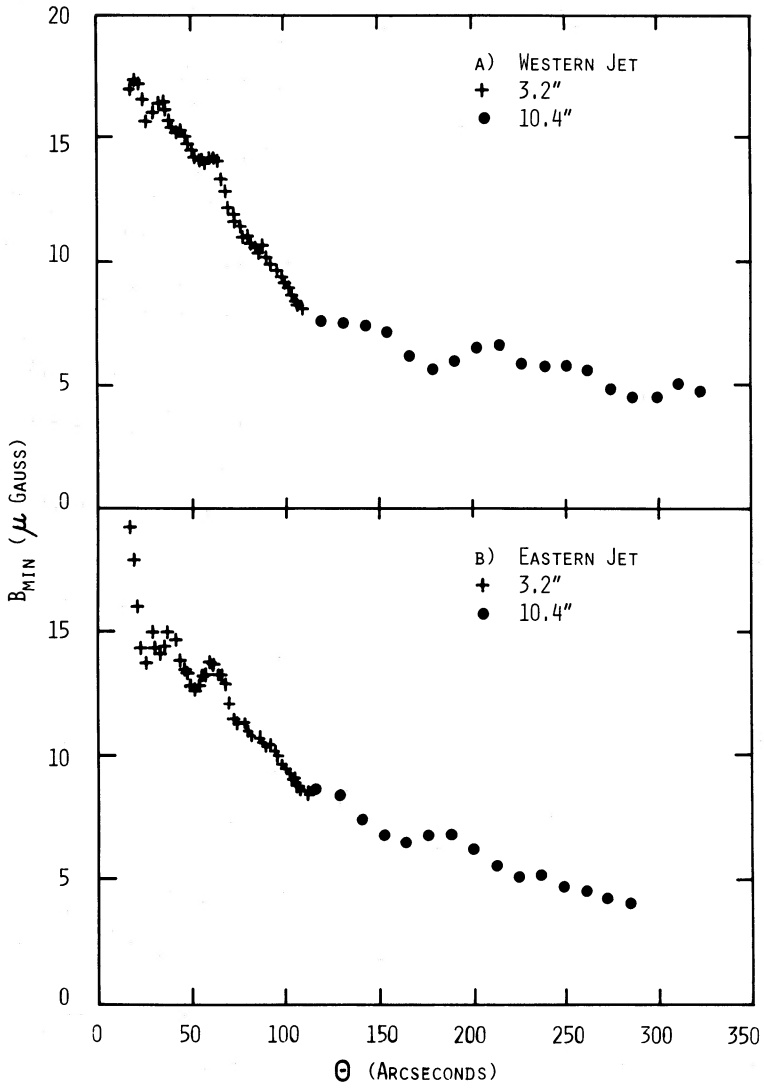

FIG. 29.—Minimum energy magnetic field along both jets: (*a*) is west; (*b*) is east. The 3.″2 resolution 20 cm map is used until $\Theta \approx 100$, whereupon the 10.″4 resolution map is used.

40%, and there is a significant enhancement in the degree of polarization at the outer edge of the western lobe.

9. The minimum energy densities (particles and fields) in the jets range from $\sim 3 \times 10^{-11}$ ergs cm^{-3} close to the core to $\sim 2 \times 10^{-12}$ ergs cm^{-3} at large Θ. Over a similar range in Θ, the minimum energy magnetic field varies from 20 to 5 μG. In the lobes, the minimum energy density is approximately 3×10^{-13} ergs cm^{-3}, and the minimum energy magnetic field is ~ 2 μG.

N.E.B.K. wishes to acknowledge financial support from the IAU Commission 38 which enabled an overseas trip to the VLA, and a Commonwealth Postgraduate Research Award. N.E.B.K. also wishes to thank the VLA personnel for making his stay there both enjoyable and fruitful. We are grateful to Alan Bridle for helpful comments on the manuscript, Peggy Perley for calibrating some of the data, and Sue Parkes for her work on the diagrams. We thank an anonymous referee for numerous comments which improved the style of this paper.

APPENDIX A

DECONVOLUTION OF SURFACE BRIGHTNESS PROFILES AND JET WIDTHS

For a cylindrical jet with a Gaussian transverse surface brightness profile and constant surface brightness along its length (see Fig. 30), the actual surface brightness is given by

$$I_\nu = I_{\nu 0} \exp\left(-0.5 x^2 \sigma_x^{-2}\right),$$

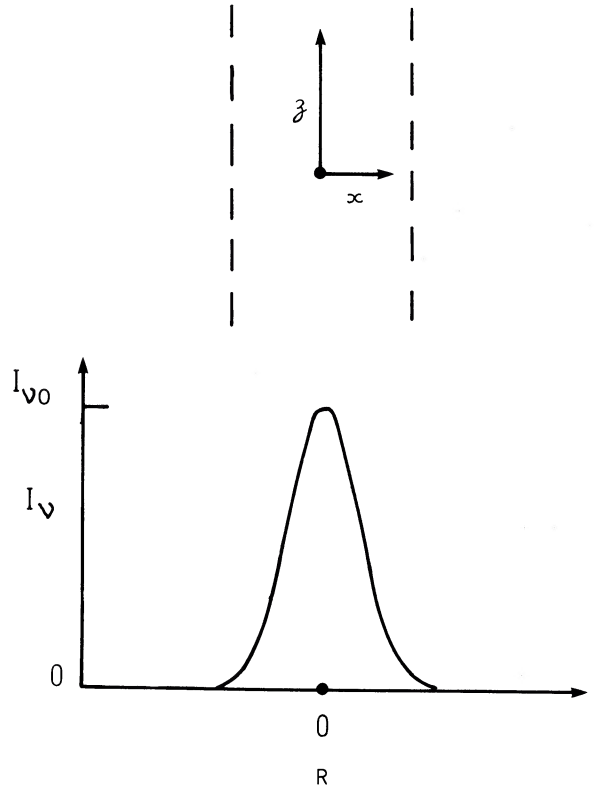

FIG. 30.—Geometry for a jet with Gaussian surface brightness. Variable z is in the direction along the axis of the jet, while x is transverse to the jet.

where x is the distance from the jet center in the transverse direction, $I_{\nu 0}$ is the surface brightness at $x = 0$, and σ_x is the standard deviation of the jet width. Convolving with a two-dimensional Gaussian (the beam) of the form $\exp [-0.5(z^2\sigma_{b,z}^{-2} + x^2\sigma_{b,x}^{-2})]$, where $\sigma_{b,z}$ is the standard deviation of the beam width in the z-direction and $\sigma_{b,x}$ is the standard deviation of the beam width in the x-direction, yields for the flux per beam

$$S_\nu = 2\pi I_{\nu 0}(\sigma_x^{-2} + \sigma_{b,x}^{-2})^{-1/2}\sigma_{b,z} \exp [-0.5x^2/(\sigma_x^2 + \sigma_{b,x}^2)] . \quad \text{(A1)}$$

Thus the actual surface brightness at a radius $x = 0$ (i.e., the surface brightness ridge line) is given by

$$I_{\nu 0} = S_{\nu 0}(2\pi\sigma_{b,x}\sigma_{b,z})^{-1}(\sigma_{b,x}^2\sigma_x^{-2} + 1)^{1/2} ,$$

or

$$I_{\nu 0} = I'_{\nu 0}(\sigma_{b,x}^2\sigma_x^{-2})^{1/2} , \quad \text{(A2)}$$

where $I'_{\nu 0}$ is the apparent surface brightness. Equation (A1) also gives for the intrinsic jet width, σ_x, the usual equation

$$\sigma_x = (\sigma_m^2 - \sigma_{b,x}^2)^{1/2} , \quad \text{(A3)}$$

where σ_m is the measured jet width. To establish a cutoff in the deconvolution, two criteria are used. We require the width of the beam to be less than the length scale of the surface brightness in the z-direction, and the measured jet width to be greater than the beam width, i.e.

$$(I_{\nu 0})^{-1}\frac{dI_{\nu 0}}{dz} \leq \Phi_b^{-1} \quad \text{and} \quad \Phi_j \geq \Phi_b , \quad \text{(A4)}$$

where Φ_b is the beam FWHM and Φ_j is the measured jet width at half-maximum.

APPENDIX B

MAXIMUM LIKELIHOOD ESTIMATE OF THE TOTAL POLARIZED INTENSITY

The probability density function $f(P')$ for the polarization P' of a signal with intrinsic polarization P is the Rice distribution (Vinokur 1965)

$$f(P';\ P,\ \sigma^2) = P'\sigma^{-2}I_0(PP'\sigma^{-2}) \exp [-0.5\sigma^{-2}(P^2 + P'^2)] , \quad \text{(B1)}$$

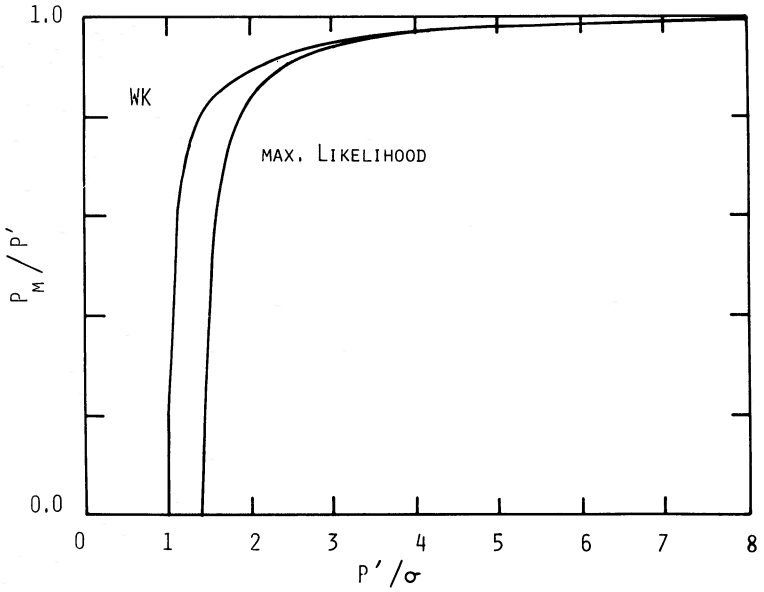

FIG. 31.—Percentage correction to the degree of polarization as a function of the signal-to-noise ratio due to Gaussian noise. Curves predicted by Wardle and Kronberg and the maximum likelihood method are both shown.

where σ^2 is the variance of the Stokes Q and U distributions (which are assumed to have identical Gaussian statistics) and I_0 is the modified Bessel function of order zero. One wishes to estimate P, given a sample of the random variable P' of size 1. Wardle and Kronberg (1974) estimated P from P' based upon the mode of $f(P)$. We prefer to use the statistically more appealing maximum likelihood estimate P_m (Kendall and Stuart, pp. 35–74) defined by

$$\frac{d}{dP_m}\left[f(P';\ P_m, \sigma^2)\right] = 0\ . \tag{B2}$$

The estimate P_m is the value of P that maximizes the probability of obtaining P'. This results in the equation

$$P_m P'\sigma^{-2} I_0(P_m P'\sigma^{-2}) - P'^2\sigma^{-2} I_1(P_m P'\sigma^{-2}) = 0\ , \tag{B3}$$

where I_1 is the modified Bessel function of order unity.

For $P'\sigma^{-1} \gg 1$ (high signal-to-noise)

$$P_m \approx P' - 0.5P'^{-1}\sigma^2\ , \tag{B4}$$

which is similar to the asymptotic expression of Wardle and Kronberg;

$$P_{\rm WK} \approx P'[1 - (P'^{-2}\sigma^2)]^{1/2}\ . \tag{B5}$$

In Figure 31 we have plotted P_m/P' against P'/σ in order to show the percentage "correction" to P' implied by the estimate P_m, as a function of the signal-to-noise P'/σ. The curve defined by equation (A2) in Wardle and Kronberg is also displayed for comparison (in their notation, we have plotted R/R' against R'_m/σ). Figure 31 indicates that our estimate P_m of P is less than the estimate of Wardle and Kronberg at low signal-to-noise.

APPENDIX C

SYNCHOTRON EMISSIVITY FOR GAUSSIAN JETS

The synchotron emissivity can be usefully expressed in terms of the relativistic electron pressure as follows. From Pacholczyk (1970), the synchotron emissivity for an ensemble of electrons is given by

$$\epsilon_\nu = c_5(a)N_0(B\sin\theta)^{(a+1)/2}(\nu/2c_1)^{(1-a)/2}\ , \tag{C1}$$

where a is the exponent of the electron number density distribution function $N(E) = N_0 E^{-a}$. The quantity $B\sin\theta$ is the component of the magnetic field perpendicular to the line of sight, ν is the frequency, and the constants c_1 and c_5 are tabulated in Pacholczyk. The scale factor N_0 in equation (C1) can be eliminated in favor of the relativistic electron pressure P_e, where

$$P_e = \frac{1}{3}\int_{E_l}^{E_u} N_0 E^{1-a} dE = \frac{N_0 E_l^{2-a}}{3(a-2)}\left[1 - \left(\frac{E_u}{E_l}\right)^{2-a}\right]. \tag{C2}$$

Expressing the upper and lower energy cutoffs E_u and E_l in terms of the critical frequencies ν_u and ν_l and substituting for N_0 in equation (C1) gives

$$\epsilon_\nu = CP_e(B \sin \theta)^{3/2}(\nu/2c_1)^{(1-a)/2} , \tag{C3}$$

where $C = 3(a-2)c_5(a)(\nu_l/c_1)^{(a-2)/2}[1-(\nu_u/\nu_l)^{(2-a)/2}]^{-1}$. Note that C does not depend strongly on ν_l, since a is typically close to 2. The surface brightness is given by

$$I_\nu = C(\nu/2c_1)^{(1-a)/2} \int P_e(B \sin \theta)^{3/2} dl ,$$

where dl is an element of the path length. By making the standard projection substitution, $r^2 = x^2 + y^2$ (see Fig. 32) the surface brightness becomes

$$I_\nu(x) = 2C(\nu/2c_1)^{(1-a)/2}(\sin \theta)^{3/2} \int_x^\infty P_e(r)B(r)^{3/2}(r^2 - x^2)^{-1/2} r dr \tag{C4}$$

for jets perpendicular to the line of sight. We now make the assumption that $P_e(r)B(r)^{3/2}$ is Gaussian of width σ. Substituting in equation (C4) gives

$$I_\nu(x) = 2C(\nu/2c_1)^{(1-a)/2} P_{ec}(B_c \sin \theta)^{3/2} \int_x^\infty \exp(-r^2/2\sigma^2)(r^2 - x^2)^{-1/2} r dr , \tag{C5}$$

where the subscript c denotes quantities at the center of the jet. The integral I^* in equation (C5) is integrated by parts to yield

$$I^* = \frac{1}{\sigma^2} \int_x^\infty \exp \frac{-r^2}{2\sigma^2} r(r^2 - x^2)^{1/2} dr ,$$

so that

$$\frac{\partial I^*}{\partial x} = \frac{-x}{\sigma^2} I^*$$

and

$$I^* = I_0^* \exp(-x^2/2\sigma^2) ,$$

where

$$I_0^* = \int_0^\infty \exp(-r^2/2\sigma^2) dr = (2\pi)^{1/2}\sigma/2 .$$

Thus, equation (C5) becomes

$$I_\nu(x) = (2\pi)^{1/2} C(\nu/2c_1)^{(1-a)/2} P_{ec}(B_c \sin \theta)^{3/2} \sigma \exp(-x^2/2\sigma^2) , \tag{C6}$$

and for the center of the jet, the exponential term is unity.

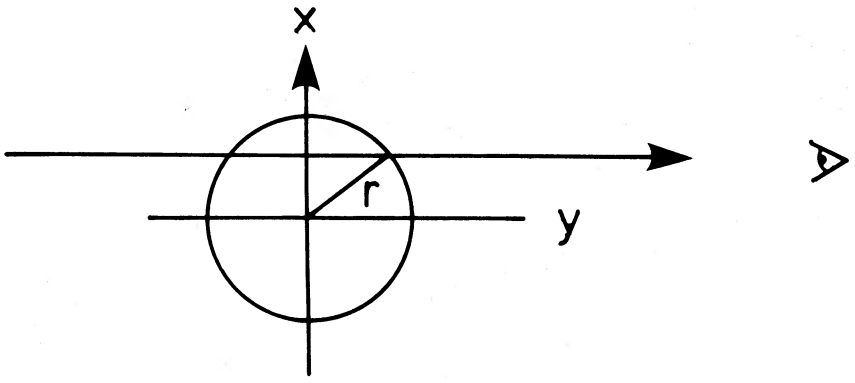

FIG. 32.—Geometry for projecting the surface brightness of a jet. Line of sight is assumed perpendicular to the jet which is seen end-on.

APPENDIX D

MINIMUM ENERGY AND PRESSURE FOR GAUSSIAN JETS

Perley, Willis, and Scott (1979) give expressions for the minimum energy parameters expressed in terms of the surface brightness and width of cylindrical jets. We give here a derivation of the minimum energy and minimum pressure equations for Gaussian jets, which produces marginally lower results than for cylindrical jets.

We write equation (C6) at the center of the jet as $P_{ec} B_c^{3/2} = K$ for brevity, where

$$K = \frac{I_{vc}}{(2\pi)^{1/2}\sigma(\sin\theta)^{3/2}C}\left(\frac{\nu}{2c_1}\right)^{(a-1)/2}.$$

In the usual manner, consider the total energy density (at the center of the jets):

$$\epsilon_{tc} = 3(1+k)P_{ec} + \phi B_c^2/8\pi = 3KB_c^{-3/2}(1+k) + \phi B_c^2/8\pi\,, \tag{D1}$$

where ϕ is the filling factor for the magnetic field and k is the ratio of the energies in relativistic protons plus thermal particles to relativistic electrons. The quantity ϵ_{tc} is minimum (as a function of B_c) when

$$\frac{B_c^2}{8\pi} = \frac{1}{8\pi}\left[\frac{18\pi K(1+k)}{\phi}\right]^{4/7}, \tag{D2}$$

so that

$$P_{ec}^{\min\,\epsilon} = KB_c^{-3/2} = [18\pi\phi^{-1}(1+k)]^{-3/7}K^{4/7}\,. \tag{D3}$$

Thus, at the minimum energy point,

$$\frac{\phi B_c^2}{8\pi} = \frac{9}{4}(1+k)P_{ec}^{\min\,\epsilon}\,.$$

It follows from this expression, equations (D1), (D3), and the expression for K (see above) that

$$\epsilon_{tc}^{\min\,\epsilon} = \frac{21}{4}\left(\frac{\phi}{18\pi}\right)^{3/7}\left[\frac{I_{vc}(1+k)}{(2\pi)^{1/2}\sigma(\sin\theta)^{3/2}c_{15}}\right]^{4/7}, \tag{D4}$$

and from equation (D2)

$$B_c^{\min\,\epsilon} = \left[18\left(\frac{\pi}{2}\right)^{1/2}\frac{I_{vc}(1+k)}{\sigma\phi(\sin\theta)^{3/2}c_{15}}\right]^{2/7}, \tag{D5}$$

where I_{vc} is the surface brightness at the center of the jet, σ is the width of the Gaussian surface brightness profile, and $c_{15} = C(\nu/2c_1)^{(1-a)/2}$ (C is defined in Appendix C).

Similarly, by considering the total pressure $P_{tc} = P_{ec}(1+k') + \phi B_c^2/8\pi$, where k' is the ratio of the pressures of the relativistic protons plus thermal particles to the relativistic electrons, and minimizing it with respect to B_c, we find

$$P_{tc}^{\min\,P} = \frac{7\phi^{3/7}}{24\pi}\left[6\left(\frac{\pi}{2}\right)^{1/2}\frac{(1+k')I_{vc}}{\sigma(\sin\theta)^{3/2}c_{15}}\right]^{4/7}. \tag{D6}$$

If $k = k'$, then

$$P_{tc}^{\min\,P} = 3^{-4/7}\epsilon_{tc}^{\min\,\epsilon}\,. \tag{D7}$$

REFERENCES

Baars, J. W. M., Genzel, R., Pauliny-Toth, I. I. C., and Witzel, A. 1977, *Astr. Ap. Suppl.*, **61**, 99.
Bicknell, G. V. 1984, *Ap. J.*, **286**, 68.
Bridle, A. H. 1982, in *IAU Symposium 97, Extragalactic Radio Sources*, ed. D. S. Heeschen and C. M. Wade (Dordrecht: Reidel), p. 121.
Bridle, A. H., and Perley, R. A. 1984, *Ann. Rev. Astr. Ap.*, **22**, 319.
Butcher, H. R., van Breugel, W., and Miley, G. K. 1980, *Ap. J.*, **235**, 749.
Clark, B. G. 1980, *Astr. Ap.*, **89**, 377.
Ekers, R. D., Shaver, P. A., Goss, W. M., Fosbury, R. A. E., Danziger, I. J., Wall, J. V., and Malin, D. 1985, preprint.
Gardner, F. F., and Davies, R. D. 1964, *Nature*, **201**, 144.
Gardner, F. F., and Whiteoak, J. B. 1971, *Australian J. Phys.*, **24**, 899.
Goss, W. M., Wellington, K. J., Christiansen, W. N., Lockhart, I. A., Watkinson, A., Frater, R. H., and Little, A. G. 1977, *M.N.R.A.S.*, **178**, 525.
Högbom, J. A. 1974, *Astr. Ap. Suppl.*, **15**, 417.
Kendall, M. G., and Stuart, A. 1979, *The Advanced Theory of Statistics*, Vol. **2** (London: Griffin).
Krautter, A., Henriksen, R. N., and Lake, K. 1983, *Ap. J.*, **264**, 81.
Linfield, R. 1981, *Ap. J.*, **244**, 436.
———. 1982, *Ap. J.*, **254**, 465.
Love, E. S., Grigsby, C. E., Lee, L. P., and Woodling, M. E. 1959, NASA Tech. Rept. No. R-6.
Miley, G. K. 1980, *Ann. Rev. Astr. Ap.*, **18**, 165.
Mills, B. Y., Slee, O. B., and Hill, E. R. 1960, *Australian J. Phys.*, **13**, 676.
Norman, M. L., Smarr, L., Winkler, K. H. A., and Smith, M. D. 1982, *Astr. Ap.*, **113**, 285.
Pacholczyk, A. G. 1970, *Radio Astrophysics* (San Francisco: Freeman).
Perley, R. A., Bridle, A. H., and Willis, A. G. 1984, *Ap. J. Suppl.*, **54**, 291.
Perley, R. A., Dreher, J. W., and Cowan, J. J. 1984, *Ap. J.* (*Letters*), **285**, L35.
Perley, R. A., Willis, R. G., and Scott, J. S. 1979, *Nature*, **281**, 437.

Readhead, A. C. S., Cohen, M. H., and Blandford, R. D. 1978, *Nature*, **272**, 131.
Schilizzi, R. T., and McAdam, W. B. 1970, *Proc. Astr. Soc. Australia*, **1**, 337.
Schwab, F. R. 1980, *SPIE Proc.*, **231**, 18.
Shaver, P. A., Danziger, I. J., Ekers, R. D., Fosbury, R. A. E., Goss, W. M., Malin, D., Moorwood, A. F. M., and Wall, J. V. 1982, in *IAU Symposium 97, Extra Galactic Radio Sources*, ed. D. S. Heeschen and C. M. Wade (Dordrecht: Reidel), p. 55.
Shimmins, A. J., Manchester, R. N., and Harris, B. J. 1969, *Australian J. Phys. Suppl.*, **8**, 1.
Simard-Normandin, M., Kronberg, P. P., and Button, S. 1981, *Ap. J. Suppl.*, **45**, 97.
Slee, O. B. 1977, *Australian J. Phys. Suppl.*, **43**, 1.
Swarup, G. 1984, *J. Ap. Astr.*, **5**, 139.
van Dyke, M. 1982, *An Album of Fluid Motion* (Stanford: Parabolic).
Vinokur, M. 1965, *Ann. d'Ap.*, **28**, 412.
Wardle, J. F. L., and Kronberg, P. P. 1974, *Ap. J.*, **194**, 249.

G. V. BICKNELL: Mount Stromlo and Siding Spring Observatories, Private Bag, Woden P.O., Canberra, A.C.T. 2606, Australia

R. D. EKERS: National Radio Astronomy Observatory, P.O. Box 0, Socorro, NM 87801

N. E. B. KILLEEN: National Radio Astronomy Observatory, Edgemont Road, Charlottesville, VA 22903-2475